

Neutron transfer reactions in halo effective field theory

M. Schmidt,^{1,2} L. Platter,^{3,4} and H.-W. Hammer^{1,5}

¹*Institut für Kernphysik, Technische Universität Darmstadt, 64289 Darmstadt, Germany*

²*Department of Physics and Astronomy,
University of Tennessee, Knoxville, TN 37996, USA*

³*Department of Physics and Astronomy,
University of Tennessee, Knoxville, Tennessee 37996, USA*

⁴*Physics Division, Oak Ridge National Laboratory,
Oak Ridge, Tennessee 37831, USA*

⁵*ExtreMe Matter Institute EMMI, GSI Helmholtzzentrum für
Schwerionenforschung GmbH, 64291 Darmstadt, Germany*

(Dated: August 9, 2021)

Abstract

Direct reaction experiments provide a powerful tool to probe the structure of neutron-rich nuclei like beryllium-11. We use halo effective field theory to calculate the cross section of the deuteron-induced neutron transfer reaction $^{10}\text{Be}(d, p)^{11}\text{Be}$. The effective theory contains dynamical fields for the beryllium-10 core, the neutron, and the proton. In contrast, the deuteron and the beryllium-11 halo nucleus are generated dynamically from contact interactions using experimental and *ab initio* input. Breakup contributions are then included by construction. The reaction amplitude is constructed up to next-to-leading order in an expansion in the ratio of the length scales characterizing the core and the halo. The Coulomb repulsion between core and proton is treated perturbatively. Finally, we compare our results to cross-section data and other calculations.

I. INTRODUCTION

Nuclear processes such as capture and transfer reactions are one focus of ongoing research at existing and forthcoming experimental facilities with radioactive ion beams [1]. However, the consistent theoretical description of such reactions in *ab initio* calculations poses significant challenges. Tremendous progress has been made for lighter systems in calculating elastic nucleus-nucleon scattering processes by combining the variational approach of the resonating group model and the no-core shell model in the no-core shell model with continuum [2]. However, for larger systems it remains a challenging task to calculate reactions in a controlled way and with reliable uncertainty estimates; see for example Refs. [3–7].

One alternative approach is to reduce the number of dynamical degrees of freedom. A process can then be described as an effective two- or three-body problem using a Lippmann-Schwinger or Faddeev equation. The remaining challenge is to model the interaction between the degrees of freedom appropriately. A reduction to the minimal degrees of freedom required to obtain a certain observable is frequently the starting point of an effective field theory (EFT) treatment of a system. EFTs can be applied if a system displays two disparate scales that can be combined to form a small expansion parameter. The large scale can for example be the excitation energy of a degree of freedom or a heavy state not included in the approach. EFT is the theory in which these high energy modes are integrated out.

Halo nuclei display such a separation of scales [8–11]. They consist of a tightly bound core with large excitation energy E_x and some weakly bound valence nucleons. The EFT that has been developed for these systems is called halo effective field theory (Halo EFT) [12, 13]. It treats the core as a fundamental degree of freedom, which is a valid approximation as long as energies smaller than E_x are considered. Halo EFT has been applied to a variety of processes including electromagnetic transitions and Coulomb dissociation of one-neutron halo nuclei. The formalism has been extended to one-proton and two-neutron halo nuclei. For a recent review, see Ref. [14].

In this work, we explore the potential of Halo EFT to describe the experimentally important process of a deuteron-induced transfer reaction. Such a calculation has not been carried out yet due to the challenging continuum structure of the reaction. As a test case, we consider $^{10}\text{Be}(d, p)^{11}\text{Be}$. The effective three-body system is given by a ^{10}Be core, a neutron, and a proton. The one-neutron halo nucleus ^{11}Be represents a neutron-core state with a binding energy much smaller than the 2^+ core excitation energy $E_x = 3.37$ MeV; see Fig. 1. This intrinsic scale separation reflects itself also in the small core radius $R_c \sim 2\text{--}3$ fm and the large halo radius $R_h \sim 7$ fm [15]. Exploiting these length scales, we construct the reaction cross section at leading order (LO) and next-to-leading order (NLO) in R_c/R_h . We find that dynamical core excitations and strong proton-core interactions can be neglected up to NLO. Deuteron and ^{11}Be breakup contributions will be included automatically since Halo EFT contains all continuum states of the active degrees of freedom (core, proton, and neutron).

We expect that the Halo EFT expansion works best for center-of-mass energies E well below $E_x = 3.37$ MeV; see Fig. 1. However, in the absence of appropriate data, we compare our theory to data at $E \geq 7.78$ MeV, measured by Schmitt *et al.* at Oak Ridge National Laboratory [17, 18]. In fact, previous works suggest that Halo EFT could still be appropriate for the lower experimental energies. For example, Deltuva *et al.* calculated the differential cross section in a Faddeev approach, using model interactions that reproduce elastic proton-core scattering data and optical potentials that account for loss channels [19]. Their work suggests that core excitations barely influence the cross section for $E \lesssim 10$ MeV. More

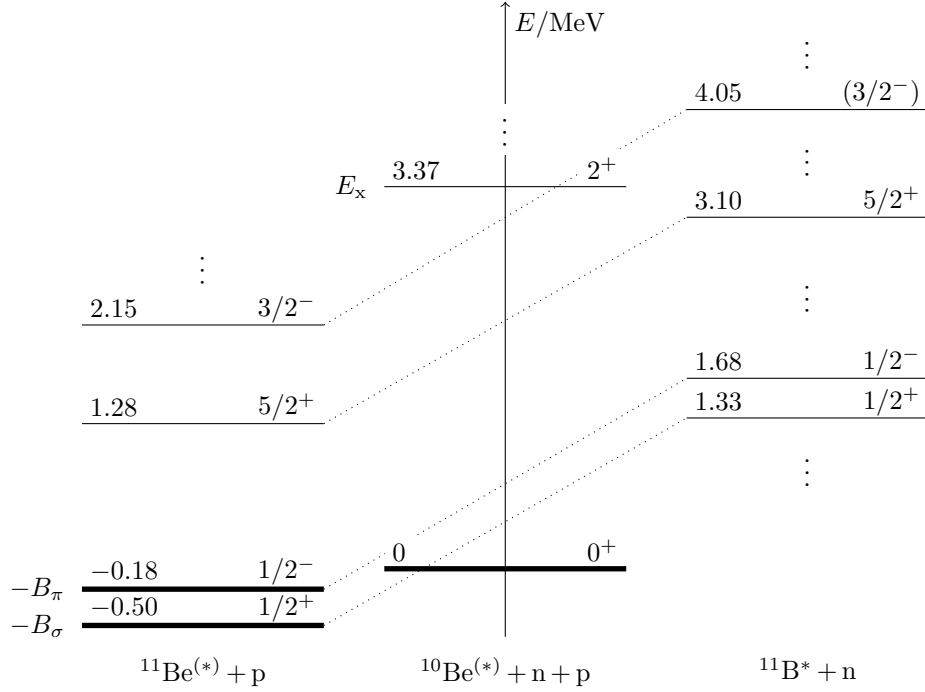


Figure 1: Thresholds relative to $^{10}\text{Be} + n + p$. The center column shows the ground and first excited state of beryllium-10. Bound and resonance states of the core-neutron (beryllium-11) and core-proton (boron-11) systems are depicted in the left and right columns, respectively. We only show ^{11}B levels, which have been seen in the $^{10}\text{Be}(p, \gamma)^{11}\text{B}$ experiment of Ref. [16]. In this work, we explicitly include those states with thick lines.

recently, Yang and Capel [20] reanalyzed the reaction by combining the adiabatic distorted wave approximation reaction model with a Halo EFT description of ^{11}Be . They found out that, for the lower beam energies and forward angles, the reaction is purely peripheral. That is, it only depends on the asymptotic form of the ^{11}Be wave function, while being independent of short-range details. Indeed, we will be able to describe data for the lower beam energies.

This manuscript is structured as follows. In Sec. II, we present the EFT Lagrangian. Strong interactions among the core, neutron, and proton are described by contact forces and the Coulomb interaction follows from photon couplings. Section III explains how the two-body states ^{11}Be , $^{11}\text{Be}^*$ and the deuteron emerge dynamically from the given interactions. We then turn to the three-body system in Sec. IV. A Faddeev equation for the reaction will be constructed up to NLO in the R_c/R_h expansion. Following work carried out for the three-nucleon sector [21, 22], the Faddeev equation will include the dominant Coulomb contributions. After discussing results for the reaction cross section, we summarize our work and give an outlook in Sec. V.

II. EFT LAGRANGIAN

The EFT Lagrangian \mathcal{L} can be written as the sum

$$\mathcal{L} = \mathcal{L}_1 + \mathcal{L}_2 + \mathcal{L}_3 + \mathcal{L}_\gamma \quad (1)$$

of one-, two-, and three-body interactions and a photon part. The one-body part reads

$$\mathcal{L}_1 = n_\alpha^\dagger \left[i\partial_0 + \frac{\nabla^2}{2m_N} \right] n_\alpha + p_\alpha^\dagger \left[iD_0 + \frac{\mathbf{D}^2}{2m_N} \right] p_\alpha + c^\dagger \left[iD_0 + \frac{\mathbf{D}^2}{2m_c} \right] c. \quad (2)$$

It introduces fields n_α , p_α ($\alpha \in \{-1/2, +1/2\}$) and c for the neutron, proton, and ^{10}Be core. They are treated as distinguishable particles. Sums over doubly appearing indices are implicit. Masses are taken to be $m_N \equiv 938.918 \text{ MeV}$ and $m_c \equiv 10 m_N$.

The photon's kinetic and gauge fixing terms are given by

$$\mathcal{L}_\gamma = -\frac{1}{4} F_{\mu\nu} F^{\mu\nu} - \frac{1}{2\xi} (\partial_\mu A^\mu - \eta_\mu \eta_\nu \partial^\nu A^\mu)^2 \quad (3)$$

with timelike unit vector $\eta_\mu = (1, \mathbf{0})^T$. We only consider Coulomb photons, which induce a static potential. The covariant derivative $D_\mu \equiv \partial_\mu + ieA_\mu \hat{Q}$ in Eq. (2) with charge operator \hat{Q} induces respective photon couplings $-ie Q_{p/c}$ with $Q_p = 1$ and $Q_c = 4$. As done in Ref. [23], we introduce a screened Coulomb photon propagator

$$iG_\gamma(\mathbf{p}) \equiv i [\mathbf{p}^2 + \lambda^2 - i\epsilon]^{-1}. \quad (4)$$

The artificial photon mass λ has to be taken to zero at the end of each calculation.

The two-body part \mathcal{L}_2 involves the auxiliary fields σ_α ($\alpha \in \{-1/2, +1/2\}$) and d_i ($i \in \{-1, 0, +1\}$) for the shallow bound states ^{11}Be and deuteron, respectively. It reads

$$\begin{aligned} \mathcal{L}_2 = & \sigma_\alpha^\dagger \left[\Delta_\sigma^{(0)} - \left(i\partial_0 + \frac{\nabla^2}{2M_{\text{Nc}}} \right) \right] \sigma_\alpha - g_\sigma [\sigma_\alpha^\dagger (n_\alpha c) + \text{H.c.}] \\ & + d_i^\dagger \left[\Delta_d^{(0)} - \left(i\partial_0 + \frac{\nabla^2}{4m_N} \right) \right] d_i - g_d C_{1/2\alpha, 1/2\beta}^{1i'} [d_{i'}^\dagger (p_\alpha n_\beta) + \text{H.c.}] \\ & + \mathcal{L}_{2,^{11}\text{Be}^*} + \dots \end{aligned} \quad (5)$$

with $M_{\text{Nc}} \equiv m_N + m_c$ and a Clebsch-Gordan coefficient $C_{s_1 m_1, s_2 m_2}^{s_3 m_3}$. The expression ‘‘H.c.’’ denotes the Hermitian conjugate. The regularization-dependent parameters $\Delta_a^{(0)}$, $g_a \in \mathbb{R}$ ($a \in \{\sigma, d\}$) will be matched to experiment. Derivatives in Eq. (5) induce range corrections at NLO. The part $\mathcal{L}_{2,^{11}\text{Be}^*}$ accounts for further NLO contributions from the first excited state $^{11}\text{Be}^*$. It is discussed in Appendix D. Higher-order terms in the ellipses are negligible at NLO.

The three-body part \mathcal{L}_3 contains an s -wave deuteron-core interaction C_0 which will be used to renormalize the LO reaction amplitude. We write

$$\mathcal{L}_3 = -g_d^2 C_0 (d_i c)^\dagger (d_i c) + \dots \quad (6)$$

III. TWO-BODY STATES

In this section, we show how ^{11}Be , $^{11}\text{Be}^*$, and the deuteron emerge dynamically from contact interactions of the EFT Lagrangian. Our approach automatically takes care of two-body breakup, a crucial ingredient for the transfer reaction due to the small neutron separation energies of deuteron and ^{11}Be ; see, for example, Refs. [24–26]. Moreover, we explain the effective treatment of core excitation effects in the ^{11}Be system.

A. The beryllium-11 ground state

In Halo EFT, the ^{11}Be ground state ($1/2^+$) is treated as a pure neutron-core s -wave state. Already at LO, its propagator, iG_σ , depicted as a solid-dashed double line in Fig. 2 (a), contains iterations of the so-called neutron-core self-energy loop to all orders. This important quantity represents a summation over all neutron-core s -wave continuum states allowed by energy-momentum conservation. Thus, breakup contributions are automatically included.

As a consequence of the EFT's Galilean invariance, iG_σ is a function of the center-of-mass energy $E_{\text{cm}} \equiv p^0 - \mathbf{p}^2/(2M_{\text{Nc}})$ only, where p^μ denotes the total four-momentum and $M_{\text{Nc}} = m_{\text{N}} + m_{\text{c}}$ is the total mass. After resumming the self-energy loop, the propagator¹ iG_σ takes the well-known effective range expansion form

$$iG_\sigma(E_{\text{cm}}) = -i g_\sigma^{-2} \frac{2\pi}{\mu_{\text{Nc}}} \left[-a_\sigma^{-1} + \frac{r_\sigma}{2} k^2 + \dots - ik \right]^{-1}, \quad (7)$$

where $\mu_{\text{Nc}} \equiv m_{\text{N}}m_{\text{c}}/(m_{\text{N}} + m_{\text{c}})$ is the reduced mass and $k \equiv i[-2\mu_{\text{Nc}}(E_{\text{cm}} + i\epsilon)]^{1/2}$ is the on-shell relative momentum [27]. In the power divergence subtraction (PDS) scheme with mass scale Λ_{PDS} [28, 29], the scattering length a_σ and effective range r_σ are connected to the Lagrangian parameters $\Delta_\sigma^{(0)}$ and g_σ of Eq. (5) by

$$a_\sigma^{-1} = \frac{2\pi}{\mu_{\text{Nc}}} \frac{\Delta_\sigma^{(0)}(\Lambda_{\text{PDS}})}{g_\sigma^2} + \Lambda_{\text{PDS}}, \quad (8)$$

$$r_\sigma = \frac{2\pi}{\mu_{\text{Nc}}^2} g_\sigma^{-2}. \quad (9)$$

The ellipses in Eq. (7) denote higher-order terms. The unitary cut term $-ik$ is a manifestation of neutron-core continuum contributions.

The propagator has a pole at $E_{\text{cm}} = -B_\sigma$, or equivalently at $k = i\gamma_\sigma$, where $B_\sigma = 0.50$ MeV [30] and $\gamma_\sigma \equiv (2\mu_{\text{Nc}}B_\sigma)^{1/2} \approx 29$ MeV are the small binding energy and binding momentum. Thus, Eq. (7) can be rearranged by writing

$$iG_\sigma(E_{\text{cm}}) = i g_\sigma^{-2} \frac{2\pi}{\mu_{\text{Nc}}} \left[\gamma_\sigma + ik - \frac{r_\sigma}{2} (k^2 + \gamma_\sigma^2) + \dots \right]^{-1}, \quad (10)$$

where we have expressed a_σ^{-1} in terms of γ_σ and r_σ .

Since the coupling g_σ is not an observable, we eliminate it using redefined auxiliary fields $\tilde{\sigma}_\alpha^{(\dagger)} \equiv g_\sigma \sigma_\alpha^{(\dagger)}$; see, for example, Ref. [31]. Consequently, we have to multiply G_σ by g_σ^2 and each (neutron-core)- ^{11}Be vertex by g_σ^{-1} .

¹ The propagator is diagonal in spin space. Respective factors $\delta^{\alpha\alpha'}$ will be omitted in the following.

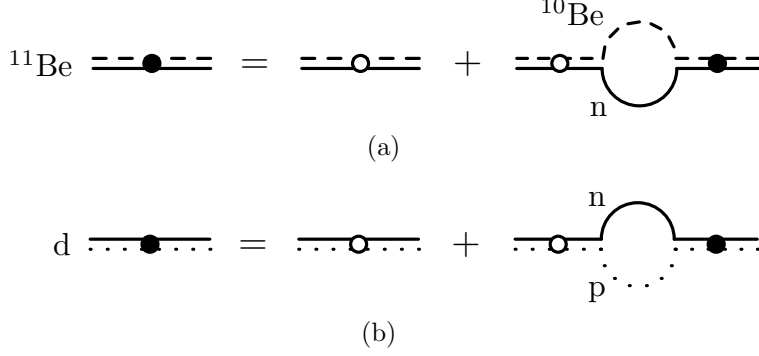


Figure 2: (a) The full ^{11}Be propagator iG_σ (solid-dashed double line with filled circle) is obtained by coupling the bare one (empty circle) to the neutron-core continuum, represented by the self-energy loop (neutron: solid line; core: dashed line). (b) Similarly, the deuteron propagator iG_d (solid-dotted double lines) couples to the neutron-proton continuum (proton: dotted line).

1. Halo EFT counting and ANC

In Halo EFT, all parameters in Eqs. (7)–(10) scale with certain powers of the large halo radius $R_h \sim 7$ fm and the small core radius $R_c \sim 2$ -3 fm. The latter represents the natural nuclear physics length scale [32]. We may estimate $R_c \sim (2\mu_{Nc}E_x)^{-1/2} \approx 2.6$ fm from the core excitation energy $E_x = 3.37$ MeV. The EFT expansion parameter is then given by $R_c/R_h \sim 0.4$.

As one of the first applications of Halo EFT to electromagnetic processes, Hammer and Phillips used data of the low-energy E1 strength of ^{11}Be breakup, to determine a value for r_σ [32]. Their result 2.7 fm scales like R_c . In contrast, the binding momentum $\gamma_\sigma \approx 29$ MeV is as small as $R_h^{-1} \approx 28$ MeV. It follows that for low momenta $k \sim \gamma_\sigma$, the effective range term $\sim R_c R_h^{-2}$ in Eq. (10) is of NLO compared to $\gamma_\sigma + ik \sim R_h^{-1}$. Higher-order terms in the ellipses are of the order $R_c^3 R_h^{-4}$ (N³LO) at most [32].

Once physics in the pole region is reproduced at a desired accuracy, it becomes obsolete to scale the ^{11}Be ground-state wave function with a spectroscopic factor. Such scheme dependent quantities are not required in Halo EFT. Instead, Eq. (10) yields an asymptotic normalization coefficient (ANC)

$$A_\sigma = \sqrt{\frac{2\gamma_\sigma}{1 - \gamma_\sigma r_\sigma + \mathcal{O}(R_c^3/R_h^3)}} \quad (11)$$

for the radial wave function $u_\sigma(r) = A_\sigma \exp(-\gamma_\sigma r)$, which is fully determined by low-energy observables [32].

Recently, Calci *et al.* were able to calculate the ANC using the no-core shell model with continuum [33]. Their result $A_\sigma = 0.786 \text{ fm}^{-1/2}$ was afterward confirmed by Yang and Capel in Ref. [20], who extracted the value $(0.785 \pm 0.03) \text{ fm}^{-1/2}$ from the cross-section data of Ref. [18]. The value was also confirmed in analyses of ^{11}Be breakup at intermediate and high energies in Refs. [4, 34]. We will use the ANC of Calci *et al.* as an input parameter at NLO. Equation (11) can then be inverted to give a value for the effective range, which reads

$$r_\sigma \equiv \left(\gamma_\sigma^{-1} - \frac{2}{A_\sigma^2} \right) (1 + \mathcal{O}(R_c^2/R_h^2)) \approx 3.5 \text{ fm}. \quad (12)$$

This value is larger than the one obtained by Hammer and Phillips in Ref. [32]. It will still be counted as R_c , since $\gamma_\sigma r_\sigma \approx 0.52$ differs by only $0.12 \lesssim (R_c/R_h)^2$ from $R_c/R_h \sim 0.4$.

2. Propagator expansion

From NLO, the propagator in Eq. (10) exhibits spurious deep poles in addition to the physical one representing ^{11}Be [35]. We solve this issue by expanding iG_σ around $k = i\gamma_\sigma$ in terms of R_c/R_h , yielding the series

$$iG_\sigma(E_{\text{cm}}) = i \frac{2\pi}{\mu_{\text{Nc}}} \left[\gamma_\sigma - \sqrt{-2\mu_{\text{Nc}}(E_{\text{cm}} + i\epsilon)} \right]^{-1} \times \left[1 + \frac{r_\sigma}{2} \left(\gamma_\sigma + \sqrt{-2\mu_{\text{Nc}}(E_{\text{cm}} + i\epsilon)} \right) + \mathcal{O}(R_c^2/R_h^2) \right]. \quad (13)$$

The residue of G_σ has an analog expansion and reads

$$Z_\sigma \equiv \left[\frac{\partial G_\sigma^{-1}}{\partial E_{\text{cm}}} \Big|_{E_{\text{cm}} = -B_\sigma} \right]^{-1} = \frac{2\pi}{\mu_{\text{Nc}}^2} \gamma_\sigma (1 + \gamma_\sigma r_\sigma + \mathcal{O}(R_c^2/R_h^2)). \quad (14)$$

In Sec. IV, G_σ will enter the three-body Faddeev equation and Z_σ is needed to normalize the reaction amplitude. At LO, we will truncate Eqs. (13)–(14) after the leading terms “1,” yielding expressions $G_\sigma^{(\text{LO})}$ and $Z_\sigma^{(\text{LO})}$. The NLO forms $G_\sigma^{(\text{NLO})}$ and $Z_\sigma^{(\text{NLO})}$ also include the terms linear in r_σ . We will follow Bedaque *et al.* by replacing $G_\sigma^{(\text{LO})} \rightarrow G_\sigma^{(\text{NLO})}$ in the Faddeev kernel at NLO [36]. This straightforward technique is often referred to as “partial resummation,” because it induces specific amplitude terms proportional to r_σ^n , $n \geq 2$. In principle, such terms only occur at higher orders. However, for natural cutoffs, they are smaller than NLO terms and do not undermine the validity of the NLO calculation [35, 37].

3. Core excitation effects

So far, we have treated ^{11}Be as a pure $1/2^+ \otimes 0^+$ neutron-core state. However, in principle, it also couples to the $1/2^+ \otimes 2^+$ configuration of a neutron and a core excitation $^{10}\text{Be}^*$ (d wave). Note that this threshold resides far above the pole at an energy separation $E_x + B_\sigma \gg B_\sigma$; see Fig. 1. Close to the pole, G_σ is insensitive to nonanalyticities of this remote channel.

Instead, it only receives residual modifications, which are automatically taken into account by renormalization onto low-energy observables γ_σ , r_σ , etc. Indeed, Deltuva *et al.* confirmed that dynamical core excitations within the ^{11}Be bound state barely influence the reaction cross section [19]. In other words, our *effective* single-channel description readily contains all the relevant core excitation information in the pole regime. For illustration, we show in Appendix A that our approach is equivalent to a theory with an explicit $^{10}\text{Be}^*$ field.

B. The beryllium-11 excited state

A second neutron-core state close to threshold is the first excited state $^{11}\text{Be}^*$ ($1/2^-$). In Halo EFT, it is treated as a p -wave bound state [32] with binding energy $B_\pi = 0.18 \text{ MeV}$

[30], or binding momentum $\gamma_\pi \equiv (2\mu_{\text{Nc}}B_\pi)^{1/2} \approx 18 \text{ MeV}$. The Lagrangian part $\mathcal{L}_{2,^{11}\text{Be}^*}$ is given in Appendix D. As shown in Ref. [12], shallow p -wave states require the inclusion of at least two low-energy parameters. Close to the pole, we choose $\gamma_\pi \sim R_h^{-1}$ and the p -wave effective range $r_\pi \sim R_c^{-1}$. The propagator expansion then reads

$$iG_\pi(E_{\text{cm}}) = i \frac{6\pi}{\mu_{\text{Nc}}} \frac{2}{-r_\pi} [\gamma_\pi^2 + 2\mu_{\text{Nc}}(E_{\text{cm}} + i\epsilon)]^{-1} (1 + \mathcal{O}(R_c/R_h)). \quad (15)$$

Similarly to the ground state, r_π can be obtained from the respective ANC A_π [32]. Taking the value $A_\pi = 0.129 \text{ fm}^{-1/2}$ of Calci *et al.* [33], we find

$$r_\pi = -\frac{2\gamma_\pi^2}{A_\pi^2} (1 + \mathcal{O}(R_c/R_h)) \approx -0.95 \text{ fm}^{-1}. \quad (16)$$

In the transfer reaction $^{10}\text{Be}(d, p)^{11}\text{Be}$, intermediate $^{11}\text{Be}^*$ states represent NLO corrections to the reaction amplitude since $G_\pi \propto R_c < R_h$, and higher orders in Eq. (15) are at most of N²LO. For the moment, we neglect the excited state. It will be subject to the NLO discussion in Sec. IV D.

C. The deuteron

The deuteron is treated as an s -wave neutron-proton bound state with binding energy $B_d = 2.22 \text{ MeV}$ [38]. The product $\gamma_d r_d \approx 0.40$ of the small binding momentum $\gamma_d \equiv (m_{\text{N}}B_d)^{1/2} \approx 46 \text{ MeV}$ and the effective range $r_d = 1.75 \text{ fm}$ [38] is as small as R_c/R_h . It follows that, up to NLO ($\sim \gamma_d r_d$), the deuteron propagator can be obtained in analogy to the one of ^{11}Be . In doing so, one also includes couplings of the deuteron propagator (solid-dotted double line) to the neutron-proton s -wave continuum; see Fig. 2 (b).

After performing field redefinitions $d_i^{(\dagger)} \rightarrow \tilde{d}_i^{(\dagger)} \equiv g_d d_i^{(\dagger)}$, expressions for the propagator² iG_d around the pole, its residue Z_d , and respective truncations can be obtained from Eqs. (13)–(14) by replacing all subscripts “ σ ” by “ d ”, the total mass M_{Nc} by $2m_{\text{N}}$, and the reduced mass μ_{Nc} by $m_{\text{N}}/2$. Relativistic effects and s - d mixing are negligible up to NLO as shown by Chen *et al.* [39].

D. Other partial wave channels

Two-body interactions in partial waves different from the ones discussed above are negligible at NLO. For example, the 1S_0 virtual state of neutron-proton scattering enters the reaction $^{10}\text{Be}(d, p)^{11}\text{Be}$ at N²LO. Neutron-proton p -wave interactions enter at N³LO due to the lack of shallow states. Strong proton-core resonances shown in Fig. 1 would also enter at N³LO. Details on how to obtain these power counting classifications in Halo EFT will be given at the end of Sec. IV D.

Even though two-body interactions are restricted to channels with shallow states, the free (noninteracting) two-body continua will be taken care of in all partial wave channels; see below. These channels are described by plane waves up to NLO.

² The deuteron propagator is diagonal in spin space, i.e., it has to be multiplied by $\delta^{ii'}$ in diagrams.

IV. THREE-BODY SYSTEM

In this section, we derive an integral integration for the reaction cross section from interactions of the Lagrangian \mathcal{L} up to NLO in the R_c/R_h expansion. First, we show which strong and Coulomb diagrams are induced by couplings of the Lagrangian \mathcal{L} . Second, we construct the LO transfer amplitude and present results for the LO cross section. At the end of the section, we discuss NLO corrections.

A. Power counting and LO diagrams

The transfer amplitude $T_{\sigma d}$ connects the two states

$$|\sigma\rangle \equiv |p + {}^{11}\text{Be}\rangle, \quad |d\rangle \equiv |{}^{10}\text{Be} + d\rangle \quad (17)$$

through neutron exchanges and Coulomb diagrams. In EFT, these diagrams can be classified in a systematic power counting, which exploits the typical momentum scales of the system.

1. Momentum scales

The typical momentum scales of the three-body system are given by the small binding momentum scale $\gamma \sim \gamma_d \sim \gamma_\sigma \sim R_h^{-1}$ and the inverse core radius R_c^{-1} . The largest subleading corrections in the strong sector are suppressed by $\gamma_\sigma r_\sigma \approx 0.52 \sim \gamma_d r_d \approx 0.40$; see above.

Coulomb diagrams additionally introduce the small ‘‘Coulomb momentum’’

$$p_c \equiv Q_c \alpha \mu_{Nc} \approx 25 \text{ MeV} \lesssim \gamma, \quad (18)$$

where $\alpha \equiv e^2/(4\pi) \approx 1/137$ is the fine structure constant. Moreover, Rupak and Kong pointed out that external momenta p have to be counted separately from γ in the presence of Coulomb photons [21]. In this work, we calculate cross sections for center-of-mass energies $E \geq 7.78 \text{ MeV}$. Thus, p is of the order $p \sim (2m_N E)^{1/2} \geq 120 \text{ MeV} > \gamma$. The two scales p_c and p form a second expansion parameter $p_c/p < 0.2$, which we will count like $(R_c/R_h)^2$.

2. Strong interaction

In Fig. 3, we display the neutron exchange diagrams that form the elementary building blocks of the strong interaction part of the transfer amplitude. We denote them by $-iV_{\sigma d}^{Sm,1m'}$ and $-iV_{d\sigma}^{1m,S'm'}$, where $S, S' \in \{0, 1\}$ and m, m' represent total incoming and outgoing spins and their projections, respectively.

Let \mathbf{p} (\mathbf{q}) be the incoming (outgoing) relative momentum³ and E the center-of-mass energy. We then find

$$V_{\sigma d}^{Sm,1m'}(\mathbf{p}, \mathbf{q}; E) = -\delta^{S1} \delta^{mm'} m_N \left[\mathbf{p} \cdot \mathbf{q} + p^2 + \frac{1+y}{2} q^2 - m_N(E + i\epsilon) \right]^{-1}, \quad (19)$$

$$V_{d\sigma}^{1m,S'm'}(\mathbf{p}, \mathbf{q}; E) = V_{\sigma d}^{S'm',1m}(\mathbf{q}, \mathbf{p}; E), \quad (20)$$

³ In this work, relative momenta in the three-body center-of-mass system are defined as the momentum of the respective spectator particle. That is, they equal $\mathbf{p}({}^{10}\text{Be}) = -\mathbf{p}(d)$ in $|d\rangle$, or $\mathbf{p}(p) = -\mathbf{p}({}^{11}\text{Be})$ in $|\sigma\rangle$.

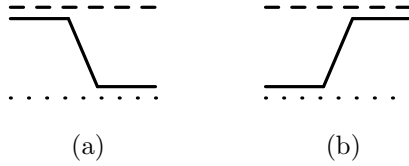


Figure 3: Neutron exchange diagrams (a) $-iV_{\sigma d}$ and (b) $-iV_{d\sigma}$. The different line types (single and double) are explained in Fig. 2. Both diagrams exhibit dynamical three-body intermediate states, coming into play via (a) ^{11}Be and (b) deuteron breakup.

where $y \equiv m_N/m_c$ is the mass ratio. Due to the s -wave nature of the short-range interactions, only transitions between spin states $S = S' = 1$ with projections $m = m'$ are possible. In the following, we will refer to the functions in Eqs. (19)–(20) as “neutron exchange potentials”.

For neutron exchanges, we use the standard power counting of pionless EFT, which counts all momenta formally like $\gamma \sim R_h^{-1}$. Loops, one-body propagators, and s -wave two-body propagators then count like γ^5/m_N , m_N/γ^2 , and $1/(\gamma m_N)$, respectively. It follows that all neutron exchange iterations are of order $m_N R_h^2$ and have to be resummed at LO.

Recall that we include deuteron and ^{11}Be breakup within the two-body-state propagators (double lines) to all orders by coupling them to continuum states as shown in Fig. 2. In three-body diagrams, further breakup contributions occur. For example, consider the diagram in Fig. 3 (a). The first⁴ (upper) vertex in this diagram describes the breakup of the incoming ^{11}Be bound state into a neutron-core pair. At this point, the initial $|\text{p} + ^{11}\text{Be}\rangle$ state evolves into an interacting $|\text{p} + \text{n} + ^{10}\text{Be}\rangle$ three-body state. Afterward, the exchanged neutron combines with the proton into a deuteron. Physically, the intermediate three-body state can be on shell since the center-of-mass energy E is positive in the experiment by Schmitt *et al.* [17, 18]. Correspondingly, Eq. (19) exhibits poles for $E > 0$.

3. Coulomb contributions

Next, we consider the Coulomb force, whose repulsion is expected to lower the reaction probability. In calculations, it is usually included as a static two-body potential in addition to some nuclear model interaction. In a strict EFT approach, however, Coulomb diagrams can be analyzed in a systematic power counting, which exploits the system’s momentum scales. This procedure reveals the relative importance of neutron exchange and Coulomb diagram interactions.

Photon couplings in \mathcal{L} induce the diagrams $-i\Gamma_{ab}^{Sm,S'm'}$ ($a, b \in \{\text{d}, \sigma\}$) in Fig. 4. Their mathematical expressions are given in Appendix C. In the following, we analyze the diagrams using the Coulomb power counting suggested by Rupak and Kong [21].

Bubble diagrams The one-loop diagrams (a) and (b) in Fig. 4 are proportional to the photon propagator ($\sim p^{-2}$) and to p_c ; see Eq. (18). All momenta in the loop (“bubble”) may be counted like γ .⁵ That is, we count one-body propagators like m_N/γ^2 and the

⁴ Time flows from left to right in our diagrams.

⁵ This statement can be verified by analyzing the bubble diagrams in the limit of zero momentum transfer, where they are largest; see Appendix C.

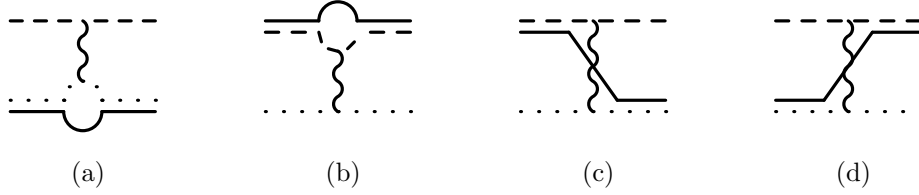


Figure 4: Coulomb diagrams entering the (a) $|\mathbf{d}\rangle$ channel, (b) $|\sigma\rangle$ channel, and [(c) and (d)] transfer channels. Curvy lines represent Coulomb photon propagators. In the LO calculation, each diagram is resummed to all orders; see Fig. 5.

loop integration by γ^5/m_N . The resulting scaling $m_N \gamma p_c/(\gamma^2 p^2)$ suggests that bubble diagrams are small compared to neutron exchanges ($\sim m_N/\gamma^2$) since $p > \gamma \gtrsim p_c$.

Box diagrams In the box diagrams of Figs. 4(c) and 4(d), the photon is part of a loop. In this case, it is not straightforward to see if the corresponding integral is governed by powers of p or γ . Since $p > \gamma$ in our case, the safest option is to count the loop like m_N/γ^3 . This scheme is in line with Ref. [22]. The overall scaling $m_N p_c/\gamma^3$ implies that box diagrams are of the same order as neutron exchanges since $p_c \lesssim \gamma$.

In summary, the Rupak and Kong counting suggests that box diagrams should be iterated at LO, while bubble diagrams are subleading ($\sim \gamma p_c/p^2$). However, one important feature of the bubble diagrams is not captured by the counting. Their photon propagators exhibit infrared divergences at small momentum transfers in the limit of vanishing photon mass; see Eqs. (C1)–(C2). In principle, this enhancement could compensate for the discussed suppression. We account for this possibility by including the bubble diagrams already in the LO calculation, as was also done in Ref. [22]. We will then critically assess this choice by comparing the numerical influence of the box and bubble diagrams on the cross section.

Note that we only consider diagrams with one photon exchange between two strong interactions. Corrections from two or more successive exchanges should be small since they involve further powers of the small Coulomb momentum p_c . In principle, they could be included by replacing each photon propagator with the full Coulomb T matrix; see for example [22]. We have checked that, for example, $-i\Gamma_{\text{dd}}$ would be modified by around 20% $\sim p_c/p \sim (R_c/R_h)^2$ in the on-shell limit. Such effects are neglected in this work.

B. Transfer amplitude at LO

By iterating neutron exchanges, Coulomb bubble diagrams, and Coulomb box diagrams to all orders, we obtain the LO transfer amplitude $T_{\sigma\mathbf{d}}^{(\text{LO})}$. The corresponding Faddeev equation (without three-body force) is shown diagrammatically in Fig. 5. Loop integrals on the right-hand side ensure that all intermediate states allowed by energy-momentum conservation are taken care of.

1. Partial wave channels

It is beneficial for our purposes to perform a partial wave projection onto the total angular momentum $\mathbf{J} = \mathbf{L} + \mathbf{S}$ with total spin S and total orbital angular momentum L .

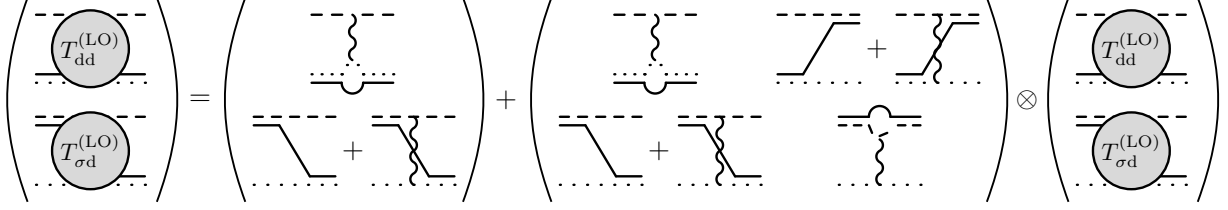


Figure 5: Transfer and elastic amplitude at LO. Loop integrals on the right-hand side contain LO propagators $G_a^{(\text{LO})}$ ($a \in \{d, \sigma\}$) (drawn without circles). The three-body force $C_0(\Lambda)$ is omitted.

This procedure is explained in Appendix B. The respective neutron exchange potentials

$$V_{\sigma d}^{2S+1L_J, 3L'_J}(p, q; E) = \delta^{S1} \delta^{LL'} \frac{m_N}{pq} Q_L \left(-\frac{p^2 + \frac{1+y}{2}q^2 - m_N(E + i\epsilon)}{pq} \right), \quad (21)$$

$$V_{d\sigma}^{3L_J, 2S'+1L'_J}(p, q; E) = V_{\sigma d}^{2S'+1L'_J, 3L_J}(q, p; E), \quad (22)$$

depend on Legendre functions of the second kind,

$$Q_L(x_0) \equiv -\frac{1}{2} \int_{-1}^1 dx \frac{P_L(x)}{x - x_0}, \quad (23)$$

in the convention of Ref. [40]. Unfortunately, partial wave expressions of the Coulomb diagram interactions are impractically lengthy. Instead, we obtain them numerically by calculating

$$\Gamma_{ab}^{2S+1L_J, 2S'+1L'_J}(p, q; E) = \delta^{LL'} \frac{1}{2} \int_{-1}^1 dx P_L(x) \Gamma_{ab}^{S0, S'0}(\mathbf{p}, \mathbf{q}; E) \quad (a \in \{d, \sigma\}) \quad (24)$$

with $x \equiv \mathbf{p} \cdot \mathbf{q}/(pq)$.

Cross sections will contain neutron exchange potentials and Coulomb contributions up to some L_{max} , at which results can be considered converged. It is worth noting that this approach does not only take care of higher partial waves between core-deuteron and proton- ^{11}Be . In fact, it automatically includes higher partial waves in each two-body sector (neutron-proton,⁶ neutron-core, proton-core) due to breakup within the $-iV_{\sigma d}$ and $-iV_{d\sigma}$ diagrams; see Fig. 3. Thus, the free two-particle continua (plane waves) are included up to L_{max} although interactions are restricted to two-body channels with shallow states.

As indicated in Fig. 5, the LO elastic and transfer amplitudes can be summarized into an amplitude vector $\vec{T}^{(\text{LO})}$. Due to the fact that the total spins $S_d = S_\sigma = 1$ and orbital angular momenta $L_d = L_\sigma \equiv L \in \{J-1, J, J+1\}$ are conserved at LO, we identify a specific partial wave system by the superscript “[L, J].” For incoming (outgoing) relative momenta p (p'), we finally obtain the scattering equations

$$\begin{aligned} \vec{T}^{(\text{LO})[L, J]}(p, p'; E) &= -\underline{\underline{K}}^{(\text{LO})[L, J]}(p, p'; E) \cdot \vec{e}_1 \\ &+ 4\pi \int \frac{dq q^2}{(2\pi)^3} \underline{\underline{K}}^{(\text{LO})[L, J]}(p, q; E) \cdot \underline{\underline{G}}^{(\text{LO})}(q; E) \cdot \vec{T}^{(\text{LO})[L, J]}(q, p'; E) \end{aligned} \quad (25)$$

⁶ For example, when the proton- ^{11}Be pair in Fig. 3 (a) is in $L = 1$, then the intermediate three-body state has $L = 1$ between the proton and an $l = 0$ neutron-core pair. This configuration can be recoupled to $L = 0$ between the core and an $l = 1$ neutron-proton pair.

with LO amplitude vector, interaction matrix, and propagator matrix

$$\vec{T}^{(\text{LO})[L,J]} \equiv \begin{pmatrix} T_{\text{dd}}^{(\text{LO})} \\ T_{\sigma\text{d}}^{(\text{LO})} \end{pmatrix}^{3L_J, 3L_J}, \quad (26)$$

$$\underline{\underline{K}}^{(\text{LO})[L,J]} \equiv \begin{pmatrix} \Gamma_{\text{dd}} & V_{\text{d}\sigma} + \Gamma_{\text{d}\sigma} \\ V_{\sigma\text{d}} + \Gamma_{\sigma\text{d}} & \Gamma_{\sigma\sigma} \end{pmatrix}^{3L_J, 3L_J}, \quad (27)$$

$$\underline{\underline{\mathcal{G}}}^{(\text{LO})} \equiv \text{diag} \left(\mathcal{G}_{\text{d}}^{(\text{LO})}, \mathcal{G}_{\sigma}^{(\text{LO})} \right), \quad (28)$$

and $\vec{e}_1 \equiv (1, 0)^T$ in channel space. For convenience, we introduced the new functions

$$\mathcal{G}_a^{(\text{N}^n\text{LO})}(q; E) \equiv G_a^{(\text{N}^n\text{LO})}(E - q^2/(2\mu_a)) \quad (a \in \{\text{d}, \sigma\}, n \in \mathbb{N}_0), \quad (29)$$

where $\mu_{\text{d}} \equiv 2m_{\text{N}}m_{\text{c}}/(2m_{\text{N}} + m_{\text{c}})$ and $\mu_{\sigma} \equiv (m_{\text{N}} + m_{\text{c}})m_{\text{N}}/(2m_{\text{N}} + m_{\text{c}})$.

The full transfer amplitude is given as a sum over the partial wave amplitudes and respective projection operators as shown in Appendix B. In all calculations, we truncate the sum at some maximal orbital angular momentum L_{max} and increase this value toward convergence. Similarly, whenever including Coulomb diagrams, we decrease the photon mass $\lambda \rightarrow 0$. We find that the cross section converges at $L_{\text{max}} = 12$ and $\lambda = 0.1$ MeV.

2. Unphysical deep bound states

To see if Eq. (25) requires a three-body force for renormalization, we have performed an asymptotic analysis for large incoming and loop momenta $p, q \gg \gamma_{\text{d}}, \gamma_{\sigma}, (m_{\text{N}}|E|)^{1/2}$ similar to Ref. [41]. In this limit, nucleon exchanges ($\sim q^{-2}$) dominate over Coulomb contributions ($\sim q^{-3}$) [22]. Thus, we may neglect the Coulomb force for the moment. It turns out that for $L \geq 1$, the potentials in Eq. (25) fall off fast enough to produce unique amplitudes solutions. In the $[L, J] = [0, 1]$ system, however, that is not the case. Instead, the amplitudes approach a power law behavior $\sim p^{-1 \pm is_0}$ with $s_0 = 0.6357$. It follows that the system exhibits an Efimov effect, i.e., a geometric spectrum of three-body bound states at energies $E = -B_{\text{d}} - B_3$ [42–44]. We note that $\exp(\pi/s_0) \approx 140$ reproduces the universal scaling factor of three distinguishable particles with mass ratio $y = 0.1$ presented in Ref. [43].

In the following, we equip Eq. (25) with a momentum cutoff $\Lambda \gg \gamma_{\text{d}}, \gamma_{\sigma}, (m_{\text{N}}|E|)^{1/2}$. The resulting spectrum is shown in Fig. 6 as dashed lines. Coulomb diagrams do not influence the large momentum behavior of the system qualitatively. They only push the Efimov states to higher cutoffs (solid lines in Fig. 6). The system will be renormalized using the three-body coupling $C_0(\Lambda)$ of Eq. (6). It enters the interaction matrix of Eq. (27) as a constant s -wave potential like

$$K_{\text{dd}}^{(\text{LO})[0,1]} \rightarrow K_{\text{dd}}^{(\text{LO})[0,1]} + C_0(\Lambda). \quad (30)$$

Note that the choice of this specific three-body force is not unique. One could also introduce it in the transfer or the $|\sigma\rangle$ elastic channel.

The quantum numbers of the Efimov states correspond to those of a $J^\pi = 1^+$ level in boron-12. Experimentally, three such states are known [45]. In a deuteron- ^{10}Be cluster picture, their binding energies $B_3^{(\text{phys})} \geq 5.77$ MeV correspond to spatial separations $R_3 = (2\mu_{\text{d}}B_3)^{-1/2} \leq 1.5$ fm of the deuteron- ^{10}Be pair. Being of the order R_c , they do not reflect a separation of scales in the three-body sector. Thus, the cluster picture is not justified

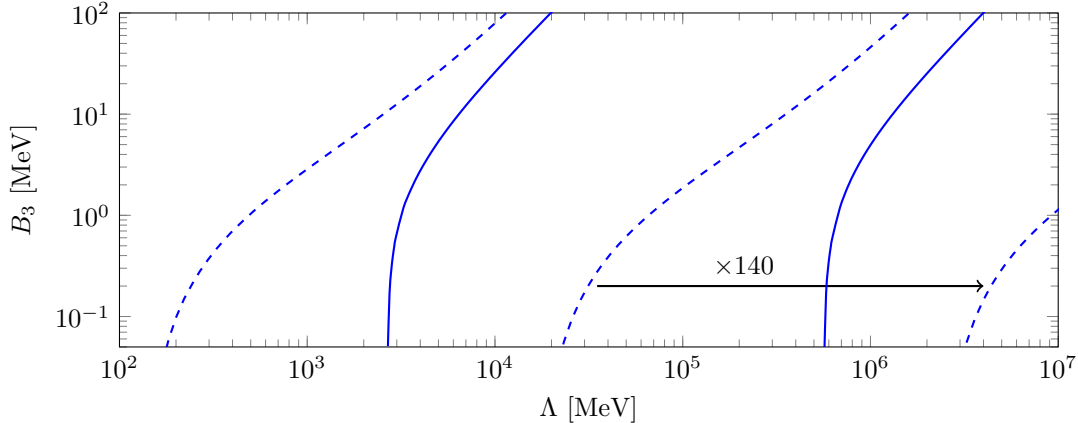


Figure 6: Unrenormalized three-body spectra at LO without (dashed lines) and with (solid lines) Coulomb diagrams ($\lambda = 0.1$ MeV, converged) for various cutoffs Λ .

and the Efimov states can be understood as artifacts of the short-range approach. However, although unphysical, they do not pose a problem as long as they lie outside the EFT's region of applicability. Indeed, after renormalization onto cross-section data, all three-body states will occur at binding energies $B_3 > 19$ MeV and thus far away from the low-energy region; see Fig. 8 (b).

C. Cross section

The differential cross section of the reaction $^{10}\text{Be}(d, p)^{11}\text{Be}$ at a deuteron beam energy

$$E_d = \frac{2m_N}{\mu_d} (E + B_d) \quad (31)$$

can be obtained by multiplying the transfer amplitude by the residue factor $(Z_\sigma Z_d)^{1/2}$ and evaluating it at on-shell relative momenta,

$$\bar{p}_a \equiv \sqrt{2\mu_a(E + B_a + i\epsilon)} \quad (a \in \{d, \sigma\}). \quad (32)$$

The cross section depends on the center-of-mass angle θ_{cm} with $\cos\theta_{\text{cm}} \equiv \hat{\mathbf{p}}(d) \cdot \hat{\mathbf{p}}(p)$. In the $|d\rangle$ channel, we set the relative momentum to $\bar{\mathbf{p}}_d \equiv -\bar{p}_d \hat{\mathbf{p}}(d)$ and in the $|\sigma\rangle$ channel we take $\bar{\mathbf{p}}_\sigma \equiv \bar{p}_\sigma \hat{\mathbf{p}}'(p)$. The spin-averaged reaction cross section then reads

$$\left(\frac{d\sigma}{d\Omega}\right)(\theta_{\text{cm}}; E) = \frac{1}{3} \sum_{m, S', m'} \frac{\mu_d \mu_\sigma \bar{p}_\sigma}{4\pi^2 \bar{p}_d} Z_d Z_\sigma \left| T_{d\sigma}^{1m, S'm'}(\bar{\mathbf{p}}_d, \bar{\mathbf{p}}_\sigma; E) \right|^2, \quad (33)$$

where $|T_{d\sigma}^{1m, S'm'}(\mathbf{p}, \mathbf{p}'; E)|^2 = |T_{\sigma d}^{S'm', 1m}(\mathbf{p}', \mathbf{p}; E)|^2$.

Table I summarizes the input parameters needed for the calculation of the reaction cross section up to NLO in the R_c/R_h expansion. At LO, only the binding energies B_d and B_σ are required. At NLO, also the effective range r_d , the ANC A_σ of ^{11}Be , and the binding energy B_π and ANC A_π of $^{11}\text{Be}^*$ enter.

Table I: EFT inputs for the calculation of the reaction cross section up to NLO in $R_c/R_h \sim 0.4$.

Order	deuteron	^{11}Be	$^{11}\text{Be}^*$
LO [$\mathcal{O}(1)$]	$B_d = 2.22 \text{ MeV}$ [38]	$B_\sigma = 0.50 \text{ MeV}$ [30]	–
NLO [$\mathcal{O}(R_c/R_h)$]	$r_d = 1.75 \text{ fm}$ [38]	$A_\sigma = 0.786 \text{ fm}^{-1/2}$ [33]	$B_\pi = 0.18 \text{ MeV}$ [30], $A_\pi = 0.129 \text{ fm}^{-1/2}$ [33]

1. Coulomb suppression and improved LO system

Our first goal is to critically assess the Coulomb power counting performed above. In particular, we would like to validate the proposed LO nature of the Coulomb force in general and of the bubble diagrams specifically, for the experimental energies used by Schmitt *et al.* [17, 18]. Given the cutoff-dependence of the $L = 0$ channel, we vary Λ in the large range $\Lambda \in [300, 1500] \text{ MeV}$ in each calculation. This procedure reveals the potential impact of the s -wave three-body force $C_0(\Lambda)$ on the LO reaction cross sections.

In a first step, we neglect all Coulomb diagrams, which yields the uppermost bands (hatched) in Fig. 7. Each curve is converged at percentage level for $L_{\text{max}} = 12$. At all four deuteron beam energies $E_d \in \{12, 15, 18, 21.4\} \text{ MeV}$ (lab frame), the bands lie high above the experimental data by Schmitt *et al.* [17, 18]. Apparently, the strong interaction alone does not produce enough repulsion between the scattering partners, even if $C_0(\Lambda)$ is included.

In order to understand the relative importance of the Coulomb box and bubble diagrams, we add them successively to the Faddeev equation. The light bands surrounded by dotted lines in Fig. 7 show that the box diagrams alone lower the cross sections drastically at all beam energies as expected. Indeed, it is important to include them at LO. Further repulsion comes from the bubble diagrams. Their inclusion yields the dark lowermost bands in Fig. 7. Apparently, the influence of the bubble diagrams on the cross section is $\lesssim 40\%$ smaller than the one of the box diagrams. Thus, it seems as if we have overestimated the enhancement due to the bubble diagrams' infrared divergences by one order in R_h/R_c . *A posteriori*, the bubble diagrams are of NLO and could in principle be neglected at LO. The “pure LO” system then only contains neutron transfer and box diagrams.

Interestingly, however, the inclusion of the bubble diagrams as one specific NLO correction leads to a surprisingly good agreement with the cross-section data at lower beam energies and forward angles. Thus, choosing the “improved LO” system of Fig. 5 significantly accelerates the EFT convergence. This statement will be verified later by including the remaining NLO corrections. Moreover, the improved LO system, unlike the pure one, can be renormalized onto data at $E_d = 12 \text{ MeV}$ since the respective band comprises all data points. We emphasize that none of the bands in Fig. (7) includes the EFT uncertainties of $\pm 40\%$ at LO; see Fig. 9 for comparison.

2. Peripherality regions

Although subleading in a strict sense, the bubble diagrams do not introduce any new parameters like, for example, effective range coefficients. Thus, the improved LO system stays independent of short-range details. Cross sections are then only affected by the tail of

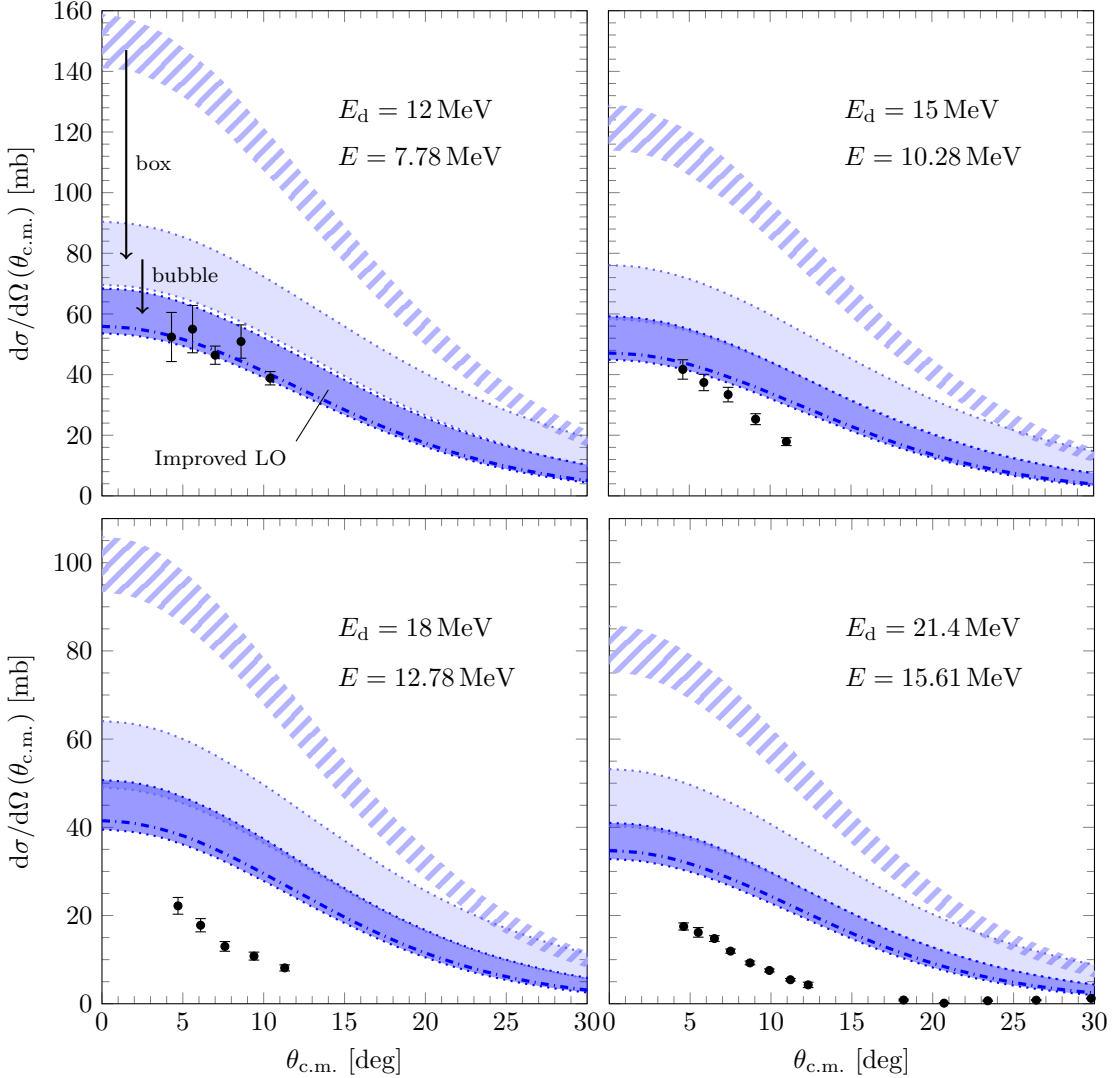


Figure 7: LO cross section of $^{10}\text{Be}(d, p)^{11}\text{Be}$ as function of the center-of mass angle θ_{cm} . For different deuteron energies E_d (lab frame), the results are compared to data (black points) from Ref. [18]. All bands are due to cutoff variations $\Lambda \in [300, 1500]$ MeV. Additional EFT uncertainties of order 40% due to neglected NLO contributions are omitted. Hatched bands exclude Coulomb contributions. Light (dark) bands enclosed by dotted lines include the Coulomb box (and bubble) diagrams. Dash-dotted curves represent a χ^2 fit of the full equation system in Fig. 5 onto the depicted $E_d = 12$ MeV data using the three-body force $C_0(\Lambda)$; see also Fig. 8. The fit is cutoff-independent for $\Lambda \geq 500$ MeV. Each single curve is converged at $L_{\text{max}} = 12$ and $\lambda = 0.1$ MeV.

the ^{11}Be wave function, i.e., the reaction is purely “peripheral”. Yang and Capel argued that such a description is sufficient to describe the reaction at lower beam energies and forward angles [20]. Our results provide clear evidence for this claim since the improved LO band for $E_d = 12$ MeV perfectly describes the whole data region ($4.7^\circ \leq \theta_{\text{cm}} \leq 10.4^\circ$).

Moreover, according to Yang and Capel, the peripherality region increases (decreases) in size for lower (higher) energies. Indeed, at $E_d = 15$ MeV, only forward scattering ($\theta_{\text{cm}} \leq 4.6^\circ$) is captured by the improved LO band. Deviations at larger angles are of NLO size. At even higher energies $E_d \geq 18$ MeV, however, the bands deviate from data by

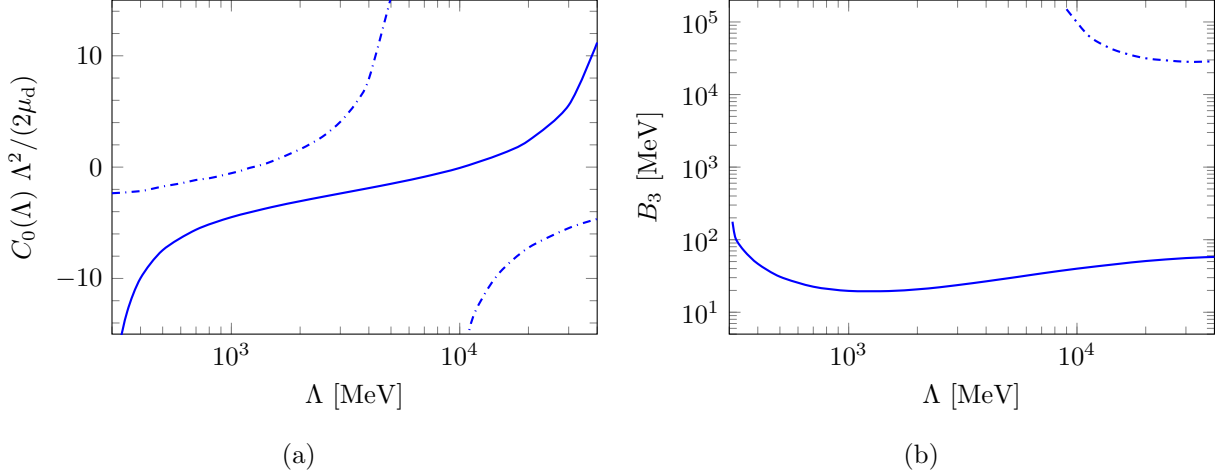


Figure 8: Renormalization of the improved LO system depicted in Fig. 5. (a) The dot-dashed and solid curves are the two solutions of $C_0(\Lambda)$ for the χ^2 fit to the $E_d = 12$ MeV data set; see Fig. 7. (b) Both solutions produce spectra outside the EFT regime, i.e., at binding energies $B_3 > 19$ MeV or $B_3 > 28$ GeV, respectively.

40-80%. We conclude that the reaction is indeed only peripheral at forward angles and low energies. For this reason our power counting may fail for energies $E_d > 15$ MeV.

Note, however, that Schmitt *et al.* identified their 18 MeV data set to be systematically smaller than the other three [18]. In particular, they extracted spectroscopic factors from all four data sets, of which the 18 MeV results were 25% smaller. Yang and Capel, who extracted the ^{11}Be ANC from the data of Schmitt *et al.*, made a similar observation [20]. Of all four data sets, only the 18 MeV set yielded an ANC 15% smaller than the prediction by Calci *et al.* [33]. Thus, our calculation might be better at 18 MeV than suggested by Fig. 7.

3. Cutoff dependence and renormalizability

Out of all components $L \leq L_{\max} = 12$, only the $L = 0$ part is cutoff-dependent. Due to this circumstance, the band widths in Fig. 7 are only 20% the size of the box diagram shift (LO). Such contributions are negligible up to NLO. Thus, in principle, each curve within the filled bands represents an LO result itself and renormalization is not required. Let us emphasize that the only inputs to our LO system are then given by the binding energies B_d and B_σ ; see Table I. At astrophysical energies, however, the $L = 0$ component is of much greater importance, leading to a much stronger cutoff dependence.

We demonstrate the renormalizability of the improved LO system using the three-body force $C_0(\Lambda)$. For various cutoffs $\Lambda \geq 300$ MeV, we adjust it in a χ^2 fit to the depicted $E_d = 12$ MeV data set. This procedure yields the two solutions for $C_0(\Lambda)$ shown in Fig. 8 (a). Their fit values $\chi^2 \approx 2.29$ (solid curve) and $\chi^2 \approx 2.23$ (dot-dashed curve) are, within numerical uncertainties, equal in size and respectively constant for $\Lambda \geq 500$ MeV. For illustration, we show fit results for $\Lambda = 500$ MeV in Fig. 7 as dot-dashed curves. The first three-body state occurs at $\Lambda \approx 300$ MeV (or $\Lambda \approx 7$ GeV); see Fig. 8 (b). It lies above $B_3 \approx 19$ MeV (or $B_3 \approx 28$ GeV) and converges to even higher values as $\Lambda \rightarrow \infty$.

D. Corrections at NLO and beyond

We now discuss NLO contributions to the reaction cross section in the R_c/R_h expansion, stemming from range corrections in the two-body sectors and from the excited state $^{11}\text{Be}^*$.

1. Effective range corrections

A straightforward way to include effective range corrections in the deuteron and ^{11}Be is to replace the LO propagators $\mathcal{G}_a^{(\text{LO})}$ by $\mathcal{G}_a^{(\text{NLO})}$ ($a \in \{d, \sigma\}$) in Eq. (25) [36].⁷ This approach reintroduces a cutoff dependence in the $L = 0$ channel. In principle, it could be cured by readjusting the three-body force $C_0(\Lambda)$ [46]. In order to see the impact of the additional cutoff dependence, we include effective range corrections in the renormalized improved LO system for various $\Lambda \in [500, 1500]$ MeV.⁸ Figure 9 shows that the resulting red hatched bands lie well within the $\pm 40\%$ LO uncertainty bands (blue, enclosed by thin solid lines) of the improved LO estimates (blue dot-dashed curves). The band widths are comparably small, giving rise to a mild cutoff dependence.

It has to be mentioned that a small fraction of the band widths stems from an unexpected cutoff dependence in the $L = 1$ sector. It can be understood as an artifact of the choice, not to perturb the amplitude itself to first order in R_c/R_h , but the integration kernel. That modifies the UV behavior of the partial wave amplitudes, leading to a divergence in the $L = 1$ sector. This divergence would not be present in a strictly perturbative approach [41]. Even though desirable, such a more involved NLO treatment lies beyond the scope of this work. In fact, we have checked that the influence of the cutoff on the $L = 1$ amplitude is less than 2% over the range $\Lambda \in [500, 1500]$ MeV. Thus, this issue can be neglected at NLO.

2. The beryllium-11 excited state

The excited state $^{11}\text{Be}^*$ introduces a third channel $|\pi\rangle \equiv |p + ^{11}\text{Be}^*\rangle$ to the three-body system. It couples to $|d\rangle$ via the diagrams $-iV_{\pi d}$, $-iV_{d\pi}$ shown in Figs. 10(a) and 10(b). Their mathematical forms and partial wave projections are given in Appendix D. We note that $|\pi\rangle$ only occurs as an intermediate state in the reaction. Thus, the NLO nature of $^{11}\text{Be}^*$ follows from the propagator scaling $G_\pi^{(\text{LO})} \sim R_c/(\gamma^2 m_N)$; see Sec. III. A typical contribution to the reaction amplitude is given by Fig. 10(c). Again, we count all loop momenta like $\gamma \sim R_h^{-1}$. The two (neutron-core)- $^{11}\text{Be}^*$ vertices contribute a factor γ^2 . The overall scaling $m_N R_c R_h$ is then one order smaller than the LO scaling $m_N R_h^2$.

We complete the NLO system by inserting both effective range corrections in G_d and G_σ , and the potentials $V_{\pi d}$, $V_{d\pi}$ into the integration kernel. The resulting Faddeev equations are given in Appendix E. Similarly to the previous calculation, we vary $\Lambda \in [500, 1500]$ MeV and include the LO three-body force $C_0(\Lambda)$. Figure 9 shows that the results of the previous calculation (hatched bands) get shifted back toward the improved LO results, ending up

⁷ Correspondingly, one has to use the residues $Z_a^{(\text{NLO})}$ in the calculation of the cross section in Eq. (33).

⁸ Below $\Lambda = 500$ MeV, the renormalized improved LO result is not yet converged. Note that the cutoff variation up to 1500 MeV is only used to estimate higher-order corrections. It does, however, not reveal the necessity of additional counter terms.

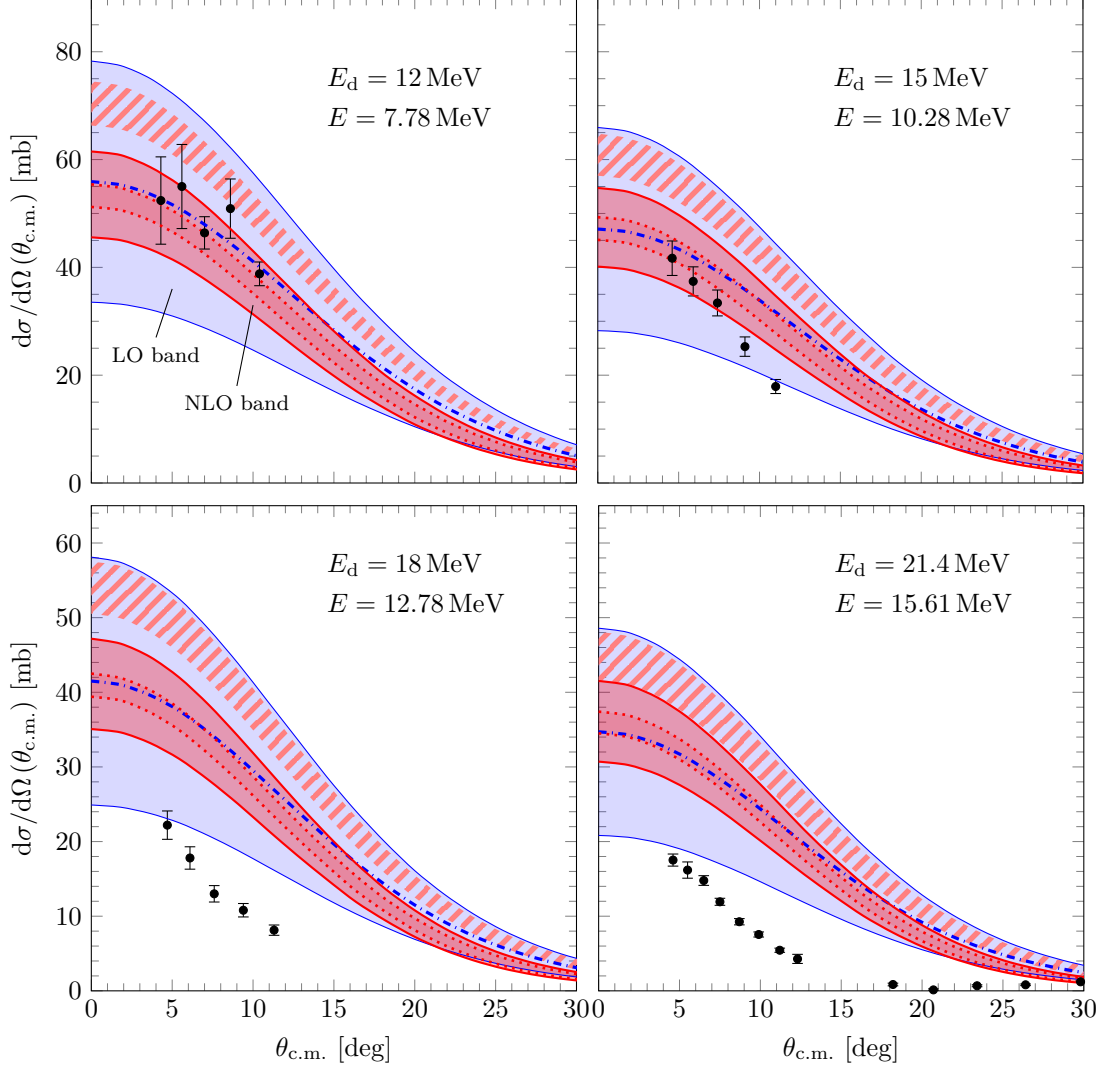


Figure 9: Cross section of $^{10}\text{Be}(d, p)^{11}\text{Be}$ up to NLO as function of the center-of-mass angle $\theta_{\text{c.m.}}$. Blue dot-dashed curves show the χ^2 fits of the improved LO system. In contrast to Fig. 7, we now vary these curves by $\pm 40\%$ to mimic neglected NLO contributions. In doing so, we obtain the blue LO bands (enclosed by thin solid lines). The red hatched bands result from effective range corrections and the red bands enclosed by dotted lines also include corrections from the excited state $^{11}\text{Be}^*$ at NLO. Both NLO calculations involve cutoff variations $\Lambda \in [500, 1500]$ MeV. The final red NLO bands (enclosed by thick solid lines) represent $\pm 16\%$ variations of the averaged NLO results due to neglected N^2LO contributions.

as red bands enclosed by dotted lines. Thus, the influence of $^{11}\text{Be}^*$ is indeed of NLO, in agreement with our power counting. The remaining cutoff dependencies of the $L = 0$ and $L = 1$ sectors are negligible compared to N^2LO corrections ($\pm 16\%$, red uncertainty bands enclosed by thick solid lines). Thus, no further renormalization is needed at NLO.

Recall that the NLO parameters $r_\sigma = 3.5$ fm and $r_\pi = -0.95$ fm $^{-1}$ were calculated in Eqs. (12) and (16) from the ANCs of Calci *et al.* [33]. Instead, one could directly use the Halo EFT values $r_\sigma = 2.7$ fm and $r_\pi = -0.66$ fm $^{-1}$ of Hammer and Phillips [32]. The relative differences 30% and 40% are of size R_c/R_h and should thus be negligible at NLO. We have

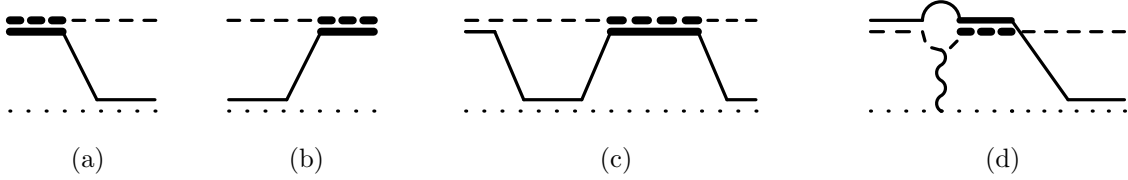


Figure 10: The one-neutron exchange diagrams (a) $-iV_{\pi d}$ and (b) $-iV_{d\pi}$ induce NLO contributions from $^{11}\text{Be}^*$ (thickened solid-dashed double line) to the transfer amplitude. The exemplary diagram in (c) contains a propagator $G_{\pi}^{(\text{LO})}$ depicted as a thickened solid-dashed double line. In (d), the intermediate $^{11}\text{Be}^*$ results from an E1 transition induced by the Coulomb field. This process is doubly suppressed by $G_{\pi}^{(\text{LO})}$ and the photon propagator and can thus be neglected at NLO.

checked that the final NLO bands would indeed only change by ca. 5%. Thus, both choices for r_{σ} , r_{π} are consistent with the proposed power counting.

In Ref. [18], the cross section for transfer to $^{11}\text{Be}^*$ was also measured. In our theory, this quantity can in principle be calculated using the amplitudes $T_{\pi d}$ in Eqs. (E1)-(E2). However, Yang and Capel found that this process is less peripheral than $^{10}\text{Be}(d, p)^{11}\text{Be}$ [20]. For this reason, we expect that our low-energy power counting has to be modified in order to describe it. Indeed, naive application of the current scheme leads to an overestimation of the data.

3. Higher-order interactions

At higher orders in Halo EFT, additional interactions would enter the calculation. For example, the proton-neutron sector exhibits a shallow 1S_0 virtual state [28, 29]. It does not occur at LO, because the total neutron-proton spin $S = 1$ is conserved if all interactions are of s -wave type. In the presence of the p -wave state $^{11}\text{Be}^*$, however, S may change, and transitions $|d\rangle \rightarrow |\pi\rangle \rightarrow |^{10}\text{Be} + np(^1S_0)\rangle$ become possible; see Fig. 11. However, the virtual state is not only suppressed due to the intermediate $|\pi\rangle$ channel. Since multiple spin changes [$\sim (R_c/R_h)^2$ or smaller] are negligible at NLO, a virtual state leads to $S = 0$ in the final state of $^{10}\text{Be}(d, p)^{11}\text{Be}$. The corresponding phase space is 1/3 the size of $S = 1$, yielding a suppression of $R_c/(3R_h) \lesssim (R_c/R_h)^2$ (N²LO).

Neutron-proton p -wave interactions are of order N³LO. The reason is the lack of a shallow neutron-proton p -wave bound or resonance state. In the $^{11}\text{Be}^*$ sector, iG_{π} approaches the large scattering volume $a_{\pi} = (457 \pm 67) \text{ fm}^3$ for small E_{cm} [47]. This large value is a consequence of the small binding momentum γ_{π} since $a_{\pi} \sim 2r_{\pi}^{-1}\gamma_{\pi}^{-2} \sim R_c R_h^2$; see Eq. (15). Scattering volumes in the neutron-proton channels 3P_2 , 3P_1 , 3P_0 , and 1P_1 are much smaller. Using the Nijmegen partial wave analysis for N-N scattering of Ref. [48], we have checked that they are all of the natural size $r_d^3 \approx 5.36 \text{ fm}^3 \sim R_c^3 \ll a_{\pi}$ or smaller (N³LO). In fact, the p -wave phase shifts themselves are suppressed compared to the 3S_1 phase shift. Even for the maximal neutron-proton center-of-mass energy $E_{\text{cm}} = 15.61 \text{ MeV}$ available in the experiment by Schmitt *et al.*, the suppression is of the order $0.09 \sim (R_c/R_h)^3$ (N³LO).

In Ref. [16], several boron-11 resonances have been observed in $^{10}\text{Be}(p, \gamma)^{11}\text{B}$; see Fig. 1. The lowest one ($1/2^+$) occurs at a proton-core center-of-mass energy $E_r = (1.33 \pm 0.04) \text{ MeV}$. It has a total width $\Gamma = (230 \pm 65) \text{ keV}$ and the branching ratio for decay into $^{10}\text{Be} + p$ is close to 1 [16]. The resonance represents a pole at $E_{\text{cm}} = E_r - i\Gamma/2$ in the Coulomb-modified

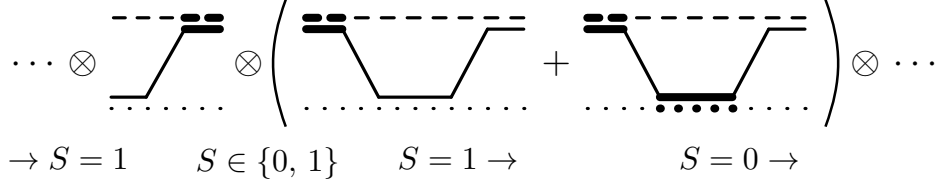


Figure 11: The excited state $^{11}\text{Be}^*$ allows transitions from total spin $S = 1$ to $S = 1$ ($|\text{d}\rangle \rightarrow |\pi\rangle \rightarrow |\text{d}\rangle$) or to $S = 0$ ($|\text{d}\rangle \rightarrow |\pi\rangle \rightarrow |^{10}\text{Be} + \text{np}(^1S_0)\rangle$). The thickened solid-dotted double line represents the neutron-proton 1S_0 virtual state. Multiple transitions via $|\pi\rangle$ are negligible at NLO.

resonance propagator; see for example Refs. [49, 50]. This pole position implies effective range terms $a_c^{-1} = ((-2.7 \pm 0.8) \text{ fm})^{-1}$ and $r_c/2(2\mu_{\text{Nc}}E_T) = ((-3.5 \pm 1.4) \text{ fm})^{-1}$, which scale like R_c^{-1} . Moreover, in three-body diagrams, the resonance propagator comes along with a Gamow-Sommerfeld factor $0 < C_\eta^2 < 1$ [51]. It gives the probability of two charged particles to meet in one point. At resonance, it takes the small value $0.13 \lesssim (R_c/R_h)^2$. It follows that the influence of the resonance propagator on the reaction is suppressed by three orders in R_c/R_h compared to iG_σ (N^3LO). Note that there are more boron-11 states around $E = 0$, which could possibly couple strongly to the proton-core system. However, transitions to those states would involve even smaller Gamow factors $C_\eta^2 < (R_c/R_h)^2$. Thus, we neglect strong proton-core interactions at NLO.

During the reaction process, the ^{11}Be state could break up into an excited core $^{10}\text{Be}^*$ and a neutron. Thus, $|\sigma\rangle$ in principle couples to the additional intermediate channel $|^{10}\text{Be}^* + \text{d}\rangle$ via neutron exchanges. However, each such channel comes along with two couplings of order R_c^2 ; see Appendix A for details. Thus, dynamical core excitations can be neglected at NLO.

Diagrams involving direct photon couplings to the auxiliary fields d_i and σ_α do not enter before N^2LO . They are one order smaller than the bubble diagrams [23], which are de facto of NLO; see above. The Coulomb field could also induce E1 transitions between ^{11}Be and $^{11}\text{Be}^*$ (or between the deuteron and a neutron-proton p -wave channel) [32]. Such a contribution is shown in Fig. 10 (d). It is negligible at NLO due to the subleading nature of the $^{11}\text{Be}^*$ propagator and due to the photon propagator, which is governed by the large external momentum scale p .

V. SUMMARY AND OUTLOOK

In this work, we carried out the first Halo EFT calculation of deuteron-induced transfer reactions. As a working example, we considered $^{10}\text{Be}(\text{d}, \text{p})^{11}\text{Be}$, involving the one-neutron halo nucleus ^{11}Be . The degrees of freedom in this approach are the ^{10}Be core, the neutron, and the proton. Strong interactions are described by contact forces alone. To obtain the differential cross section, the reaction amplitude was constructed diagrammatically in an expansion in the ratio $R_c/R_h \sim 0.4$ of core and halo radius. The corresponding Faddeev equation contains all dynamical features of a transfer reaction including two-body breakup contributions. A three-body force ensures internal consistency. We included the Coulomb force by considering the dominant photon exchange diagrams, which were iterated to all orders in the Faddeev equation.

The differential cross section was compared to experimental data by Schmitt *et al.* [17, 18]. In agreement with Yang and Capel [20], who calculated the cross section in the adiabatic

distorted wave approximation, we found that Halo EFT is able to describe scattering at low beam energies $E_d \lesssim 15$ MeV (center-of-mass energies $E \lesssim 10$ MeV). In this regime, the reaction can be considered peripheral, i.e., it predominantly depends on the long-range tail of the ^{11}Be wave function. This part is systematically reproduced by the R_c/R_h expansion.

Our theory contains only few information on the spectra of the involved particles. We included, in particular, only two-body states with a binding momentum γ clearly smaller than the respective momentum scale of short-range physics; see Fig. 1. The influence of such states should be enhanced by powers of γ^{-1} compared to those far away from the two-body threshold. As a consequence of this reduction, we were able to describe data using only a minimal amount of experimental input. At LO in the R_c/R_h expansion, only the binding energies of deuteron and ^{11}Be are needed; see Table I. NLO corrections arise from respective effective ranges and the first excited state $^{11}\text{Be}^*$. The effective ranges of the ^{11}Be states were extracted from the ANCs of the *ab initio* calculation by Calci *et al.* [33]. Both NLO corrections modify the cross section at a 40 % level, as predicted by the power counting.

While our results describe data at $E_d \lesssim 15$ MeV fairly well, they strongly overestimate the cross section at higher beam energies. Apparently, the low-energy expansion of Halo EFT converges, if at all, slowly at these energies. In order to improve the expansion, it might be necessary to modify the three-body power counting, which, at the moment, counts loop momenta like small binding momenta. In a more sophisticated power counting, tailored to beam energies $E_d > 12$ MeV, neglected higher-order interactions might already occur at lower orders. Such a scheme should be developed in the future. Hints on missing ingredients can be inferred from previous theoretical analyses, e.g., by Schmitt *et al.* in Ref. [18], Deltuva *et al.* in Ref. [19], or Yang and Capel in Ref. [20], which were successful in describing also scattering for $E_d \geq 15$ MeV. The model used in Ref. [20] contains the same amount of information on the ^{11}Be spectrum as our work. Thus, we do not expect the inclusion of beryllium-11 levels beyond the first excited state to be of prime importance.

Instead, core excitations following ^{11}Be breakup and two-body interactions in higher partial waves might provide enough absorption to lower cross sections at higher energies. Moreover, we might need to consider not explicitly measured loss channels, in particular due to deep boron-11 states indicated in Fig. 1, at these energies. Usually, such effects are included using optical model potentials, adjusted to, for example, proton-core scattering data. In the future, we will instead introduce imaginary contact terms to the strong Lagrangian, a method called ‘‘Open EFT’’ [52]. It was applied successfully to a broad range of inelastic processes including quarkonium decays in nonrelativistic QCD [53] and three-body recombinations of ultracold atoms [54].

Let us emphasize again, that Halo EFT is ideally suited for the description of strong interactions at low energies. In this sense, our long-term goal is to apply the developed framework to the astrophysical regime. While Coulomb effects become nonperturbative then, short-range effects should become less important. In this context, it will be interesting to calculate the cross section for $^{10}\text{Be}(d, p)^{11}\text{Be}^*$, which was measured in by Schmitt *et al.* [17, 18]. This process is less peripheral than $^{10}\text{Be}(d, p)^{11}\text{Be}$ [20], which is why naive application of the current power counting at experimental energies leads to an overestimation of the data. At very small energies, however, the power counting should be appropriate. Note, however, that certain Coulomb diagrams involving $^{11}\text{Be}^*$, which we could neglect for $^{10}\text{Be}(d, p)^{11}\text{Be}$, would become important for $^{10}\text{Be}(d, p)^{11}\text{Be}^*$. Moreover, we could apply the framework to other deuteron-induced reactions like $^{14}\text{C}(d, p)^{15}\text{C}$.

Acknowledgments

We thank D. R. Phillips for giving valuable feedback on the manuscript and S. König for providing information on the calculation of the Coulomb box diagrams. M. S. appreciates stimulating discussions with I. Thompson, D. Baye, and other participants of the INT Program INT-17-1a “Toward Predictive Theories of Nuclear Reactions Across the Isotopic Chart.” Moreover, M. S. sincerely thanks the Nuclear Theory groups of UT Knoxville and Oak Ridge National Laboratory for their kind hospitality and support during his research stay. This work has been funded by the Deutsche Forschungsgemeinschaft (DFG, German Research Foundation), Projektnummer 279384907, SFB 1245, by the National Science Foundation under Grant No. PHY-1555030, by the Bundesministerium für Bildung und Forschung (BMBF) through Contract No. 05P18RDFN1, and by the Office of Nuclear Physics, U.S. Department of Energy under Contract No. DE-AC05-00OR22725.

Appendix A: Core excitation effects

In this section, we show that core excitation effects in the pole region are taken care of in this work due to renormalization onto low-energy observables. For that, we consider a theory with an explicit $^{10}\text{Be}^*$ field C_m ($m \in \{-2, \dots, 2\}$) by adding a piece

$$\mathcal{L}_{1,^{10}\text{Be}^*} = C_m^\dagger \left[\partial_0 + \frac{\nabla^2}{2m_c} - E_x \right] C_m \quad (\text{A1})$$

to the Lagrangian. A similar approach has been chosen by Zhang *et al.* to analyze effects of the core excitation $^7\text{Li}^*$ on the $^7\text{Li}(n, \gamma)^8\text{Li}$ reaction [55]. Moreover, Zhang *et al.* and Ryberg *et al.* used a $^7\text{Be}^*$ core excitation field in their calculations of the S -factor of $^7\text{Be}(p, \gamma)^8\text{B}$ [56, 57]. In both systems, the core excitation occurs at low energies. That, however, is not true in our case where $(2\mu_{\text{Nc}}E_x)^{1/2} \sim R_c^{-1}$ is large.

Together with a neutron, $^{10}\text{Be}^*$ couples to the ^{11}Be ground state in a d -wave. In terms of the redefined field $\tilde{\sigma}_\alpha$, we thus write

$$\mathcal{L}_{2,^{10}\text{Be}^*} = - \sum_{s \in \{3/2, 5/2\}} \frac{g_{\sigma,x}^{(s)}}{g_\sigma} C_{1/2\alpha, 2m}^{sm_s} C_{2m_l, sm_s}^{1/2\alpha'} \left[\tilde{\sigma}_{\alpha'}^\dagger \left(n_\alpha \left\{ -i \overleftrightarrow{\nabla} \right\}_{2m_l} C_m \right) + \text{H.c.} \right]. \quad (\text{A2})$$

The vertex term contains a Galilei-invariant derivative $\overleftrightarrow{\nabla} \equiv \mu_{\text{Nc}}(m_{\text{N}}^{-1} \overleftarrow{\nabla} - m_c^{-1} \overrightarrow{\nabla})$. It is embedded in the tensor structure

$$\{\mathcal{O}\}_{lm_l} \equiv \sqrt{\frac{4\pi}{2l+1}} |\mathcal{O}|^l Y_l^{m_l}(\hat{\mathcal{O}}) \quad (\text{A3})$$

with $l = 2$, where $Y_l^{m_l}(\hat{\mathcal{O}})$ denotes a spherical harmonic, evaluated at $\hat{\mathcal{O}} \equiv \mathcal{O}/|\mathcal{O}|$.

The mass difference $E_x + B_\sigma \gg B_\sigma$ in the transition is of natural size. Thus, we assume no fine-tuning in this scattering channel and count $g_{\sigma,x}^{(s)} \sim R_c^{3/2}$. It follows that the overall couplings $g_{\sigma,x}^{(s)}/g_\sigma \sim R_c^2$ are natural as well, since $g_\sigma \sim r_\sigma^{-1/2} \sim R_c^{-1/2}$; see Eq. (9).

The core excitation modifies the ^{11}Be propagator through the $^{10}\text{Be}^*$ -neutron self-energy loop $-i\Sigma_{\sigma,x} \delta^{\alpha\alpha'}$. It resembles the ^{10}Be -neutron self-energy loop of Fig. 2, but the core line

has to be replaced by a core excitation line. Using the PDS scheme, we find

$$\begin{aligned} \Sigma_{\sigma,x}(E_{\text{cm}}) &= - \sum_s \left(\frac{g_{\sigma,x}^{(s)}}{g_\sigma} \right)^2 \frac{\mu_{\text{Nc}}}{10\pi} [2\mu_{\text{Nc}}(E_{\text{cm}} - E_x + i\epsilon)]^2 \\ &\quad \times \left(\Lambda_{\text{PDS}} - [-2\mu_{\text{Nc}}(E_{\text{cm}} - E_x + i\epsilon)]^{1/2} \right) \end{aligned} \quad (\text{A4})$$

$$\equiv -g_\sigma^{-2} \sum_n \Delta_{\sigma,x}^{(n)}(E_{\text{cm}} + i\epsilon)^n. \quad (\text{A5})$$

Note that $\Sigma_{\sigma,x}$ is analytic for $E_{\text{cm}} < E_x$, i.e., it can be expanded at $E_{\text{cm}} = 0$. The resulting coefficients $\Delta_{\sigma,x}^{(n)}$ then contribute to the unrenormalized parameters $\Delta_\sigma^{(n)}$ ($\Delta_\sigma^{(1)} \equiv -1$) of the bare ^{11}Be propagator; see Eq. (5). Thus, renormalization onto observables γ_σ (or a_σ), r_σ , etc. automatically takes care of core excitation effects at small E_{cm} , where the pole is located. In other words, C_m does not introduce any new information to the two-body sector and can be integrated out.

Appendix B: Partial wave expansion

Let us consider a general interaction \mathcal{I} , which could be an amplitude T , a neutron exchange potential V or a Coulomb diagram interaction Γ . We expand \mathcal{I} in tensor spherical harmonics

$$(\mathbf{Y}_{(L,S)Jm_J}(\hat{\mathbf{p}}))^m \equiv \sum_{m_L} C_{Lm_L,Sm}^{Jm_J} Y_L^{m_L}(\hat{\mathbf{p}}) \quad (\text{B1})$$

by writing

$$\mathcal{I}^{Sm,S'm'}(\mathbf{p}, \mathbf{q}; E) = \sum_J \sum_{L,L'} \mathcal{I}^{2S+1L_J, 2S'+1L'_J}(p, q; E) P_{2S+1L_J, 2S'+1L'_J}^{m,m'}(\hat{\mathbf{p}}, \hat{\mathbf{q}}), \quad (\text{B2})$$

$$P_{2S+1L_J, 2S'+1L'_J}^{m,m'}(\hat{\mathbf{p}}, \hat{\mathbf{q}}) \equiv 4\pi \sum_{m_J} (\mathbf{Y}_{(L,S)Jm_J}(\hat{\mathbf{p}}))^m (\mathbf{Y}_{(L',S')Jm_J}(\hat{\mathbf{q}}))^{m'*}. \quad (\text{B3})$$

Specific partial waves can be extracted via

$$\mathcal{I}^{2S+1L_J, 2S'+1L'_J}(p, q; E) = \frac{(4\pi)^{-2}}{2J+1} \sum_{m,m'} \int_{\Omega_{\mathbf{p}}, \Omega_{\mathbf{q}}} P_{2S'+1L'_J, 2S+1L_J}^{m',m}(\hat{\mathbf{q}}, \hat{\mathbf{p}}) \mathcal{I}^{Sm,S'm'}(\mathbf{p}, \mathbf{q}; E). \quad (\text{B4})$$

Appendix C: Coulomb diagrams

The Coulomb diagrams in Fig. 4 resemble such considered by König *et al.* for the three-nucleon system [23]. However, they exhibit nontrivial dependencies on the mass ratio

$y \equiv m_N/m_c$. The bubble interactions read

$$\Gamma_{\text{dd}}^{1m,1m'}(\mathbf{p}, \mathbf{q}; E) = \delta^{mm'} \frac{Q_c \alpha m_N^2}{(\mathbf{p} - \mathbf{q})^2 + \lambda^2 - i\epsilon} \times f\left(\mathbf{p} - \mathbf{q}, \mathcal{A}_d(p; E), \mathcal{A}_d(q; E)\right), \quad (\text{C1})$$

$$\Gamma_{\sigma\sigma}^{Sm,S'm'}(\mathbf{p}, \mathbf{q}; E) = \delta^{SS'} \delta^{mm'} \frac{Q_c \alpha (2\mu_{Nc})^2}{(\mathbf{p} - \mathbf{q})^2 + \lambda^2 - i\epsilon} \times f\left(\frac{y}{\xi}(\mathbf{p} - \mathbf{q}), \mathcal{A}_\sigma(p; E), \mathcal{A}_\sigma(q; E)\right), \quad (\text{C2})$$

$$= \underbrace{\left(\sqrt{\mathcal{A}_\sigma(q; E)} - \sqrt{\mathcal{A}_\sigma(p; E)}\right)}_{\left(\mathcal{A}_\sigma(q; E) - \mathcal{A}_\sigma(p; E)\right)} + \mathcal{O}(y^2)$$

and the box interactions are given by

$$\Gamma_{\sigma\text{d}}^{Sm,1m'}(\mathbf{p}, \mathbf{q}; E) = -Q_c \alpha m_N V_{\sigma\text{d}}^{Sm,1m'}(\mathbf{p}, \mathbf{q}; E) \times \left[f\left(\mathbf{p} - y\mathbf{q}, \xi^2 \mathcal{A}_\sigma(p; E), \mathcal{A}_d(q; E)\right) - \frac{\lambda}{\mathbf{p} \cdot \mathbf{q} + p^2 + \xi q^2 - m_N(E + i\epsilon)} + \mathcal{O}(\lambda^2) \right], \quad (\text{C3})$$

$$\Gamma_{\text{d}\sigma}^{1m,S'm'}(\mathbf{p}, \mathbf{q}; E) = \Gamma_{\sigma\text{d}}^{S'm',1m}(\mathbf{q}, \mathbf{p}; E), \quad (\text{C4})$$

where we defined $\xi \equiv (1 + y)/2$. Moreover, $\alpha \equiv e^2/(4\pi) \approx 1/137$ is the fine structure constant and $Q_c = 4$ is the core charge. All interactions involve the function

$$f(\Delta, \mathcal{A}_1, \mathcal{A}_2) \equiv \frac{1}{|\Delta|} \tan^{-1}\left(\frac{\mathcal{A}_1 - \mathcal{A}_2 + \Delta^2/4}{|\Delta| \sqrt{\mathcal{A}_2}}\right) + [\mathcal{A}_1 \leftrightarrow \mathcal{A}_2], \quad (\text{C5})$$

whose arguments involve the expressions

$$\mathcal{A}_d(p; E) \equiv \frac{1 + 2y}{4} p^2 - m_N(E + i\epsilon) \xrightarrow{\text{on shell}} \gamma_d^2, \quad (\text{C6})$$

$$\mathcal{A}_\sigma(p; E) \equiv \xi^{-2} \frac{1 + 2y}{4} p^2 - \xi^{-1} m_N(E + i\epsilon) \xrightarrow{\text{on shell}} \gamma_\sigma^2. \quad (\text{C7})$$

The form of $\Gamma_{\sigma\sigma}$ can be simplified significantly by neglecting terms of order $\mathcal{O}(y^2)$; see Eq. (C2). This approximation is justified since $y^2 = 0.01$ is a tiny number. The only angular dependence then comes from the photon propagator, which can be projected onto certain partial waves analytically.

The bubble diagrams $-i\Gamma_{\text{dd}}^{1m,1m'}$ and $-i\Gamma_{\sigma\sigma}^{Sm,S'm'}$ are linear in the Coulomb propagator. Thus, their largest contributions to the transfer reaction comes from the region of small momentum transfers $\mathbf{p} - \mathbf{q}$. For $\mathbf{p} = \mathbf{q}$, the values of the function f in Eqs. (C1)–(C2) collapse to $[\mathcal{A}_a(p; E)]^{-1/2}/2 \xrightarrow{\text{on shell}} 1/(2\gamma_a)$ ($a \in \{d, \sigma\}$). Thus, the deuteron and halo loops of the LO bubble diagrams in Fig. 4 may be counted like m_N/γ .

The Coulomb diagram interactions Γ_{ab} can be connected to the s -wave projected functions K_{bubble} and K_{box} of Ref. [23] by taking the limits $y, Q_c \rightarrow 1$. We find

$$\int_{-1}^1 dx \Gamma_{aa}^{10,10}(\mathbf{p}, \mathbf{q}; E) \Big|_{y, Q_c \rightarrow 1} = -\frac{m_N}{4\pi} K_{\text{bubble}}(E; p, q) \quad (a \in \{d, \sigma\}), \quad (\text{C8})$$

$$\int_{-1}^1 dx \Gamma_{\sigma d}^{10,10}(\mathbf{p}, \mathbf{q}; E) \Big|_{y, Q_c \rightarrow 1} = -\frac{m_N}{2\pi} K_{\text{box}}(E; p, q), \quad (\text{C9})$$

where $x \equiv \mathbf{p} \cdot \mathbf{q}/(pq)$.

Appendix D: Excited state of beryllium-11

In this section, we discuss the inclusion of the excited state $^{11}\text{Be}^*$ at NLO in the reaction calculation. The Lagrangian part

$$\begin{aligned} \mathcal{L}_{^{11}\text{Be}^*} = & \pi_\alpha^\dagger \left[\Delta_\pi^{(0)} + \left(i\partial_0 + \frac{\nabla^2}{2M_{\text{Nc}}} \right) \right] \pi_\alpha \\ & - g_\pi C_{1/2\alpha, 1m_l}^{1/2\alpha'} \left[\pi_{\alpha'}^\dagger \left(n_\alpha \left\{ -i \overleftrightarrow{\nabla} \right\}_{1m_l} c \right) + \text{H.c.} \right] + \dots \end{aligned} \quad (\text{D1})$$

of Eq. (5) contains an auxiliary field π_α ($\alpha \in \{-1/2, 1/2\}$) for $^{11}\text{Be}^*$ with renormalization-dependent parameters $\Delta_\pi^{(0)}, g_\pi \in \mathbb{R}$. The Galilei-invariant derivative $\overleftrightarrow{\nabla}$ and the p -wave tensor structure $\{\mathcal{O}\}_{1m_l}$ are defined in Appendix A. Unlike in the s -wave case, both the constant and derivative part of the bare propagator term in Eq. (D1) are needed to describe the shallow p -wave state [12, 32]. The full $^{11}\text{Be}^*$ propagator can be obtained by resumming all two-body loops, similarly to Fig. 2. For more details, we refer to Ref. [32]. After proper renormalization and field redefinitions $\pi_\alpha^{(\dagger)} \rightarrow \tilde{\pi}_\alpha^{(\dagger)} \equiv g_\pi \pi_\alpha^{(\dagger)}$, the propagator G_π around the pole at $E_{\text{cm}} = -B_\pi$ is given by Eq. (15).

In the NLO three-body system, the intermediate state $|\pi\rangle \equiv |p + ^{11}\text{Be}^*\rangle$ couples to $|d\rangle$ via neutron exchange potentials shown in Fig. 10. They read

$$\begin{aligned} V_{\pi d}^{Sm, 1m'}(\mathbf{p}, \mathbf{q}; E) = & m_N \sqrt{6} \begin{Bmatrix} S & 1 & 1 \\ 1/2 & 1/2 & 1/2 \end{Bmatrix} \\ & \times \frac{\sum_{m_l} C_{1m_l, 1m'}^{Sm} \left\{ \frac{1}{1+y} \mathbf{p} + \mathbf{q} \right\}_{1m_l}^*}{\mathbf{p} \cdot \mathbf{q} + p^2 + \frac{1+y}{2} q^2 - m_N(E + i\epsilon)}, \end{aligned} \quad (\text{D2})$$

$$V_{d\pi}^{1m, S'm'}(\mathbf{p}, \mathbf{q}; E) = \left[V_{\pi d}^{S'm', 1m}(\mathbf{q}, \mathbf{p}; E) \right]^* \quad (\text{D3})$$

with $S \in \{0, 1\}$ in the $|\pi\rangle$ channel and involve a $6j$ symbol. Partial wave projections are

Subsystem	$L_d = L_\sigma$	$S_d = S_\sigma$	L_π	S_π
(1)	J	1	$J \pm 1$	1
(2a)	$J - 1$	1	J	$\bar{3} \propto \sqrt{J+1} \times 3 + \sqrt{J} \times 1$
(2b)	$J + 1$	1	J	$\bar{1} \propto -\sqrt{J} \times 3 + \sqrt{J+1} \times 1$

Table II: Subsystems of fixed J after including the excited state channel $|\pi\rangle$. Subsystems (1) and (2a) require $J \geq 1$. The quantum numbers $\bar{3}$ and $\bar{1}$ in subsystems (2a) and (2b) refer to rotated spin states of $|\pi\rangle$; see Eq. (D6).

given by

$$\begin{aligned}
V_{\pi d}^{2S+1L_J 3L'_J}(p, q; E) &= (-1)^{J+1} \sqrt{2(2S+1)(2L+1)(2L'+1)} \\
&\times C_{L_0, L'0}^{10} \begin{Bmatrix} S & 1 & 1 \\ 1/2 & 1/2 & 1/2 \end{Bmatrix} \begin{Bmatrix} S & 1 & 1 \\ L' & L & J \end{Bmatrix} \\
&\times \frac{m_N}{pq} \left[\frac{1}{1+y} p Q_{L'} + q Q_L \right] \left(-\frac{p^2 + \frac{1+y}{2} q^2 - m_N(E+i\epsilon)}{pq} \right), \quad (D4)
\end{aligned}$$

$$V_{d\pi}^{3L_J 2S'+1L'_J}(p, q; E) = V_{\pi d}^{2S'+1L'_J 3L_J}(q, p; E). \quad (D5)$$

A direct transition potential between $|\sigma\rangle$ and $|\pi\rangle$ is not induced by the Lagrangian, i.e., these states can only be connected via an intermediate state $|d\rangle$.

The Clebsch-Gordan coefficient and the $6j$ symbols in Eq. (D4) imply some selection rules. First, only transitions with $|\Delta L| = 1$ are allowed. It follows that for $J = 0$, we have $L_d = L_\sigma = 1, L_\pi = 0$, and for fixed $J \geq 1$, the system decouples into the two subsystems (1) $L_d = L_\sigma = J, L_\pi = J \pm 1$ and (2) $L_d = L_\sigma = J \pm 1, L_\pi = J$. Second, $S_\pi = 1$ is fixed in subsystem (1), while both options $S_\pi \in \{0, 1\}$ are allowed in subsystem (2). Last, in subsystem (2), the two channels $L_d = L_\sigma = J \pm 1$ further decouple after defining rotated spin states

$$\begin{pmatrix} |\pi, \bar{3}J_J\rangle \\ |\pi, \bar{1}J_J\rangle \end{pmatrix} \equiv \frac{1}{\sqrt{2J+1}} \begin{pmatrix} \sqrt{J+1} & \sqrt{J} \\ -\sqrt{J} & \sqrt{J+1} \end{pmatrix} \begin{pmatrix} |\pi, {}^3J_J\rangle \\ |\pi, {}^1J_J\rangle \end{pmatrix}. \quad (D6)$$

Note that $\bar{3} = 3$ and $\bar{1} = 1$ for $J = 0$. The corresponding partial wave potentials read

$$\begin{aligned}
V_{\pi d}^{\bar{2}\mp\bar{1}J_J, {}^3(J\pm 1)J}(p, q; E) &= \mp \frac{1}{\sqrt{3}} \\
&\times \frac{m_N}{pq} \left[\frac{1}{1+y} p Q_{J\pm 1} + q Q_J \right] \left(-\frac{p^2 + \frac{1+y}{2} q^2 - m_N(E+i\epsilon)}{pq} \right), \quad (D7)
\end{aligned}$$

$$V_{d\pi}^{3(J\pm 1)J, \bar{2}\mp\bar{1}J_J}(p, q; E) = V_{\pi d}^{\bar{2}\mp\bar{1}J_J, {}^3(J\pm 1)J}(q, p; E). \quad (D8)$$

In summary, for fixed $J \geq 1$, we find the three decoupled subsystems (1), (2a), and (2b) presented in Table III. Just as in the LO case, they can be identified by the conserved quantum number (1) $L_d = J$, (2a) $L_d = J - 1$, and (2b) $L_d = J + 1$. In the case $J = 0$, only system (2b) is allowed.

Appendix E: NLO equations

As explained in Appendix D, the introduction of the excited state $^{11}\text{Be}^*$ produces three decoupled scattering systems for fixed $J \geq 1$, corresponding to $L_d = L_\sigma \in \{J-1, J, J+1\}$, and a single system for $J = 0$ with $L_d = L_\sigma = 1$. The respective NLO amplitude vectors $\vec{T}^{(\text{NLO})[L_d, J]}$ read

$$\vec{T}^{(\text{NLO})[J, J]} = \begin{pmatrix} T_{\text{dd}}^{(\text{NLO})^{3J, 3J}} \\ T_{\sigma\text{d}}^{(\text{NLO})^{3J, 3J}} \\ T_{\pi\text{d}}^{3(J-1)J, 3J} \\ T_{\pi\text{d}}^{3(J+1)J, 3J} \end{pmatrix} \quad (J \geq 1), \quad (\text{E1})$$

$$\vec{T}^{(\text{NLO})[J\pm 1, J]} = \begin{pmatrix} T_{\text{dd}}^{(\text{NLO})^{3(J\pm 1)J, 3(J\pm 1)J}} \\ T_{\sigma\text{d}}^{(\text{NLO})^{3(J\pm 1)J, 3(J\pm 1)J}} \\ T_{\pi\text{d}}^{2\mp 1 J, 3(J\pm 1)J} \end{pmatrix} \quad (J \geq 0 \text{ and } J \geq 1). \quad (\text{E2})$$

They are determined by the interaction and propagator matrices

$$\underline{\underline{K}}^{(\text{NLO})[J, J]} = \begin{pmatrix} \Gamma_{\text{dd}}^{3J, 3J} & (V_{\text{d}\sigma} + \Gamma_{\text{d}\sigma})^{3J, 3J} & V_{\text{d}\pi}^{3J, 3(J-1)J} & V_{\text{d}\pi}^{3J, 3(J+1)J} \\ (V_{\sigma\text{d}} + \Gamma_{\sigma\text{d}})^{3J, 3J} & \Gamma_{\sigma\sigma}^{3J, 3J} & 0 & 0 \\ V_{\pi\text{d}}^{3(J-1)J, 3J} & 0 & 0 & 0 \\ V_{\pi\text{d}}^{3(J+1)J, 3J} & 0 & 0 & 0 \end{pmatrix}, \quad (\text{E3})$$

$$\underline{\underline{\mathcal{G}}}^{(\text{NLO})[J, J]} = \text{diag} \left(\mathcal{G}_{\text{d}}^{(\text{NLO})}, \mathcal{G}_{\sigma}^{(\text{NLO})}, \mathcal{G}_{\pi}^{(\text{LO})}, \mathcal{G}_{\pi}^{(\text{LO})} \right), \quad (\text{E4})$$

and

$$\underline{\underline{K}}^{(\text{NLO})[J\pm 1, J]} = \begin{pmatrix} \Gamma_{\text{dd}}^{3(J\pm 1)J, 3(J\pm 1)J} & (V_{\text{d}\sigma} + \Gamma_{\text{d}\sigma})^{3(J\pm 1)J, 3(J\pm 1)J} & V_{\text{d}\pi}^{3(J\pm 1)J, 2\mp 1 J} \\ (V_{\sigma\text{d}} + \Gamma_{\sigma\text{d}})^{3(J\pm 1)J, 3(J\pm 1)J} & \Gamma_{\sigma\sigma}^{3(J\pm 1)J, 3(J\pm 1)J} & 0 \\ V_{\pi\text{d}}^{2\mp 1 J, 3(J\pm 1)J} & 0 & 0 \end{pmatrix}, \quad (\text{E5})$$

$$\underline{\underline{\mathcal{G}}}^{(\text{NLO})[J\pm 1, J]} = \text{diag} \left(\mathcal{G}_{\text{d}}^{(\text{NLO})}, \mathcal{G}_{\sigma}^{(\text{NLO})}, \mathcal{G}_{\pi}^{(\text{LO})} \right), \quad (\text{E6})$$

respectively, similar to Eq. (25). The propagator function $\mathcal{G}_{\pi}^{(\text{LO})}$ is defined via Eq. (29) with $a = \pi$ and reduced mass $\mu_{\pi} = \mu_{\sigma} = m_{\text{N}}(m_{\text{N}} + m_{\text{c}})/(2m_{\text{N}} + m_{\text{c}})$.

-
- [1] C. Fahlender and B. Jonson, Phys. Scripta **T152**, 010301 (2013).
 - [2] P. Navrátil *et al.*, Phys. Scripta **91**, 053002 (2016), 1601.03765.
 - [3] K. Yoshida, M. Gómez-Ramos, K. Ogata, and A. M. Moro, Phys. Rev. **C97**, 024608 (2018), 1711.04458.
 - [4] P. Capel, D. R. Phillips, and H.-W. Hammer, Phys. Rev. **C98**, 034610 (2018), 1806.02712.
 - [5] G. B. King, A. E. Lovell, and F. M. Nunes, Phys. Rev. **C98**, 044623 (2018), 1810.06129.
 - [6] F. M. Nunes *et al.*, EPJ Web Conf. **178**, 03001 (2018).

- [7] A. E. Lovell and F. M. Nunes, Phys. Rev. **C97**, 064612 (2018), 1801.06096.
- [8] M. V. Zhukov *et al.*, Phys. Rept. **231**, 151 (1993).
- [9] P. G. Hansen, A. S. Jensen, and B. Jonson, Ann. Rev. Nucl. Part. Sci. **45**, 591 (1995).
- [10] B. Jonson, Phys. Rep. **389**, 1 (2004).
- [11] A. S. Jensen, K. Riisager, D. V. Fedorov, and E. Garrido, Rev. Mod. Phys. **76**, 215 (2004).
- [12] C. A. Bertulani, H.-W. Hammer, and U. van Kolck, Nucl. Phys. **A712**, 37 (2002), nucl-th/0205063.
- [13] P. F. Bedaque, H.-W. Hammer, and U. van Kolck, Phys. Lett. B **569**, 159 (2003), nucl-th/0304007.
- [14] H.-W. Hammer, C. Ji, and D. R. Phillips, J. Phys. **G44**, 103002 (2017), 1702.08605.
- [15] W. Nörtershäuser *et al.*, Phys. Rev. Lett. **102**, 062503 (2009), 0809.2607.
- [16] D. R. Goosman, E. G. Adelberger, and K. A. Snover, Phys. Rev. **C1**, 123 (1970).
- [17] K. T. Schmitt *et al.*, Phys. Rev. Lett. **108**, 192701 (2012), 1203.3081.
- [18] K. T. Schmitt *et al.*, Phys. Rev. **C88**, 064612 (2013), 1311.3205.
- [19] A. Deltuva, A. Ross, E. Norvaišas, and F. M. Nunes, Phys. Rev. **C94**, 044613 (2016), 1610.04448.
- [20] J. Yang and P. Capel, Phys. Rev. **C98**, 054602 (2018), 1805.12074.
- [21] G. Rupak and X. Kong, Nucl. Phys. **A717**, 73 (2003), nucl-th/0108059.
- [22] S. König, H. W. Griedhammer, and H.-W. Hammer, J. Phys. **G42**, 045101 (2015), 1405.7961.
- [23] S. König, H. W. Griedhammer, H.-W. Hammer, and U. van Kolck, J. Phys. **G43**, 055106 (2016), 1508.05085.
- [24] M. Yilmaz and B. Gonul, Few Body Syst. **29**, 223 (2000), nucl-th/0105012.
- [25] M. Gomez-Ramos and A. M. Moro, Phys. Rev. **C95**, 044612 (2017), 1702.04954.
- [26] A. Di Pietro *et al.*, Phys. Rev. Lett. **105**, 022701 (2010).
- [27] H. A. Bethe, Phys. Rev. **76**, 38 (1949).
- [28] D. B. Kaplan, M. J. Savage, and M. B. Wise, Phys. Lett. **B424**, 390 (1998), nucl-th/9801034.
- [29] D. B. Kaplan, M. J. Savage, and M. B. Wise, Nucl. Phys. **B534**, 329 (1998), nucl-th/9802075.
- [30] TUNL Nuclear Data Evaluation Project, Energy Level Diagram, ^{11}Be (2012), URL http://www.tunl.duke.edu/nucldata/figures/11figs/11_02_2012.pdf.
- [31] H. W. Griedhammer, Nucl. Phys. **A744**, 192 (2004), nucl-th/0404073.
- [32] H.-W. Hammer and D. R. Phillips, Nucl. Phys. **A865**, 17 (2011), 1103.1087.
- [33] A. Calci *et al.*, Phys. Rev. Lett. **117**, 242501 (2016), 1608.03318.
- [34] L. Moschini and P. Capel, Phys. Lett. **B790**, 367 (2019), 1807.07537.
- [35] C. Ji, D. R. Phillips, and L. Platter, Annals Phys. **327**, 1803 (2012), 1106.3837.
- [36] P. F. Bedaque, G. Rupak, H. W. Griedhammer, and H.-W. Hammer, Nucl. Phys. **A714**, 589 (2003), nucl-th/0207034.
- [37] C. Ji and D. R. Phillips, Few Body Syst. **54**, 2317 (2013), 1212.1845.
- [38] J. de Swart, C. Terheggen, and V. Stoks (1995), arXiv:nucl-th/9509032.
- [39] J.-W. Chen, G. Rupak, and M. J. Savage, Nucl. Phys. **A653**, 386 (1999), nucl-th/9902056.
- [40] M. Abramowitz and I. A. Stegun, Handbook of Mathematical Functions (Dover, New York, 1964).
- [41] H. W. Griedhammer, Nucl. Phys. **A760**, 110 (2005), nucl-th/0502039.
- [42] V. Efimov, Phys. Lett. **33B**, 563 (1970).
- [43] E. Braaten and H.-W. Hammer, Phys. Rept. **428**, 259 (2006), cond-mat/0410417.
- [44] P. Naidon and S. Endo, Rept. Prog. Phys. **80**, 056001 (2017), 1610.09805.
- [45] TUNL Nuclear Data Evaluation Project, Energy Level Diagram, ^{12}B (2017), URL <http://>

www.tunl.duke.edu/nuclldata/figures/12figs/12_02_2017.pdf.

- [46] H.-W. Hammer and T. Mehen, Phys. Lett. **B516**, 353 (2001), nucl-th/0105072.
- [47] S. Typel and G. Baur, Phys. Rev. Lett. **93**, 142502 (2004), nucl-th/0406068.
- [48] V. G. J. Stoks, R. A. M. Klomp, C. P. F. Terheggen, and J. J. de Swart, Phys. Rev. **C49**, 2950 (1994), nucl-th/9406039.
- [49] L. P. Kok, J. W. de Maag, H. H. Brouwer, and H. van Haeringen, Phys. Rev. **C26**, 2381 (1982).
- [50] X. Kong and F. Ravndal, Phys. Lett. **B450**, 320 (1999), [Erratum: Phys. Lett. B **458**, 565 (1999)], nucl-th/9811076.
- [51] X. Kong and F. Ravndal, Phys. Lett. **B470**, 1 (1999), nucl-th/9904066.
- [52] E. Braaten, H.-W. Hammer, and G. P. Lepage, Phys. Rev. D **94**, 056006 (2016), 1607.02939.
- [53] G. T. Bodwin, E. Braaten, and G. P. Lepage, Phys. Rev. **D51**, 1125 (1995), [Erratum: Phys. Rev. D **55**, 5853 (1997)], hep-ph/9407339.
- [54] E. Braaten and H.-W. Hammer, Phys. Rev. Lett. **87**, 160407 (2001), cond-mat/0103331.
- [55] X. Zhang, K. M. Nollett, and D. R. Phillips, Phys. Rev. **C89**, 024613 (2014), 1311.6822.
- [56] X. Zhang, K. M. Nollett, and D. R. Phillips, Phys. Rev. **C89**, 051602 (2014), 1401.4482.
- [57] E. Ryberg, C. Forssén, H.-W. Hammer, and L. Platter, Eur. Phys. J. **A50**, 170 (2014), 1406.6908.